MONTAN
UNIVERSITÄT
LEOBEN

Chair of Materials Physics

Master's Thesis

Simultaneously increasing strength and ductility of nano-crystalline Cu-Zn-alloys made from powderous raw materials

Georg Holub, BSc

February 2023

MONTANUNIVERSITÄT LEOBEN
www.unileoben.ac.at

EIDESSTATTLICHE ERKLÄRUNG

Ich erkläre an Eides statt, dass ich diese Arbeit selbständig verfasst, andere als die angegebenen Quellen und Hilfsmittel nicht benutzt, und mich auch sonst keiner unerlaubten Hilfsmittel bedient habe.

Ich erkläre, dass ich die Richtlinien des Senats der Montanuniversität Leoben zu "Gute wissenschaftliche Praxis" gelesen, verstanden und befolgt habe.

Weiters erkläre ich, dass die elektronische und gedruckte Version der eingereichten wissenschaftlichen Abschlussarbeit formal und inhaltlich identisch sind.

Datum 20.02.2023

Unterschrift Verfasser/in
Georg Holub

Acknowledgements

I would like to express my deepest gratitude to my supervisor Prof. Daniel Kiener, the Chair of Material Physics of the Montanuniversität Leoben, and the European Research Council, without whom this work would not have been possible. I'm also extremely grateful to Klemens Schmuck for his ongoing help and support over the months.

Special thanks should also go to Klemens Schmuck and Michael Burtscher, for their help with the TEM measurements.

Lastly, I'd like to mention my family, who supported my studies over all these years.

This work was supported by the European Research Council (ERC) in the framework of the project "TOUGHIT - Tough Interface Tailored Nanostructured Metals" (grant agreement no.: 771146).

Contents

Abstract 1

Kurzfassung 3

List of Abbreviations 5

List of Figures 6

1 Introduction 9

2 Theoretical background 11

- 2.1 Dislocations 11
  - 2.1.1 Burgers-vector 11
  - 2.1.2 Movement of dislocations 12
  - 2.1.3 Work hardening 13
  - 2.1.4 Partial dislocations and stacking faults 14
- 2.2 Deformation in nano-crystalline materials 16
  - 2.2.1 Grain-boundary sliding and grain rotation 17
  - 2.2.2 Dislocation emission and annihilation at grain-boundaries 17
  - 2.2.3 Partial dislocation emission and mechanical twinning 17
- 2.3 Ball milling 20
- 2.4 High-pressure torsion 22
- 2.5 Tensile testing 23

2.6 X-ray diffraction 26

2.7 Scanning electron microscopy 29

3 Material synthesis and characterization 33

3.1 Sample preparation 33

3.2 Tensile testing 35

3.3 Microstructure analysis 36

4 Results and discussion 37

4.1 Part I: Parameterstudy for tensile sample fabrication 37

4.1.1 Ball milling 37

4.1.2 High-pressure torsion 39

4.2 Part II: Investigation of the different compositions 41

4.2.1 Microhardness testing 41

4.2.2 Tensile testing 43

4.2.3 Grain size and twin density measurements 45

5 Conclusions 49

6 Outlook 51

References 53

Appendix 57

Abstract

Nano-crystalline materials produced by severe plastic deformation tend to exhibit superior strength compared to their coarse-grained counterparts. Their ductility, however, stays disappointingly low. Studies have shown that alloying can reduce the stacking fault energy, thus enable additional deformation mechanisms, such as mechanical twinning. Building on former investigations of Zhao *et al.*, this work shows the utilization of this principle for samples produced by ball milling and high-pressure torsion. Powders in compositions of pure Cu, and Cu with 10, 20, and 30 wt.% Zn were used as raw materials. Saturation of the microstructure was determined by Vickers hardness measurements and by scanning electron microscope imaging, while the grain size was analyzed by transmission electron microscopy investigations. Further, tensile tests were performed to measure the mechanical properties. Despite the same compositions and therefore the same stacking fault energies as in the references, the fabricated samples showed smaller mean grain sizes and an increased tendency for twinning. Thus, improved values for yield-strength and ultimate strength for compositions up to 20 wt.% Zn, as well as significantly higher total elongations for compositions up to 10 wt.% Zn could be achieved.

Kurzfassung

Im Vergleich zu ihren grobkörnigen Gegenstücken zeigen nanokristalline Werkstoffe, welche mittels plastischer Hochverformung hergestellt wurden, oft exzellente Festigkeiten. Die Duktilität bleibt hingegen vergleichsweise gering. Frühere Studien haben gezeigt, dass die Stapelfehlerenergie durch Legieren herabgesetzt und dadurch zusätzliche Verformungsmechanismen, wie mechanische Zwillingsbildung, ermöglicht werden können. Diese Arbeit zeigt, aufbauend auf früheren Untersuchungen von Zhao *et al.*, die Anwendung dieses Prinzips auf Proben, welche mittels Mahlen in einer Kugelmühle sowie Hochdruck-Torsionsumformung hergestellt wurden. Als Ausgangsmaterial dienten Pulver mit Zusammensetzungen von reinem Cu und Cu mit 10, 20 und 30 gew.% Zn. Die Sättigung der Mikrostruktur wurde mittels Vickers Härteprüfung und Rasterelektronenmikroskopie nachgewiesen, während die Korngrößenverteilung durch Transmissionselektronenmikroskopie bestimmt wurde. Weiters wurden Zugversuche durchgeführt, um die mechanischen Eigenschaften zu bestimmen. Obwohl Zusammensetzung, und damit auch Stapelfehlerenergie, identisch mit den Referenzproben sind, zeigen die hergestellten Proben geringere mittlere Korngrößen und eine gesteigerte Tendenz zur Verzwilligung. Dadurch war es möglich, höher Werte für Streckgrenze und Zugfestigkeit bei Zusammensetzungen bis zu 20 gew.% Zn, sowie signifikant höhere Bruchdehnungen für Zusammensetzungen bis 10 gew.% Zn zu erreichen.

List of Abbreviations

BSE	Backscattered electrons
COD	crystallography open database
DDS	device deformation system
fcc	face-centered cubic
FWHM	full width at half maximum
HPT	high-pressure torsion
NC	nano-crystalline
SE	Secondary electrons
SEM	scanning electron microscope/microscopy
SPD	severe plastic deformation
TEM	transmission electron microscope/microscopy
XRD	x-ray diffraction

List of Figures

1.1 Stress-strain curves of tensile experiments conducted by Zhao *et al.* on samples with compositions of pure Cu and CuZn with 10 and 30 wt.% Zn produced by HPT and cold rolling [8]. 10

2.1 Geometry of (a) an edge dislocation, and (b) a screw dislocation. The line DC represents the dislocation line, and ABCD the additional plane of atoms in the edge dislocation [11]. 12

2.2 Burgers-loop in (a) a crystal that contains a dislocation, and (b) a dislocation-free crystal. The circle and the cross mark start and finish of the Burgers-loop, s indicates the dislocation line, and b the Burgers-vector [12]. 12

2.3 Movement of an edge dislocation across a slip plane. The arrows indicate the direction of the applied shear-stress, and the numbers 1 to 3 mark individual atoms [11]. 13

2.4 Piled up dislocations at the grain-boundary and activation of a secondary dislocation source in the neighboring grain. τ represents the external shear stress, D the grain diameter, S_1 the primary-, and S_2 the secondary dislocation source [12]. 14

2.5 Shockley-partial dislocations: (a) Splitting of a perfect dislocation with burgers-vector $\boldsymbol{b}$ into two partial dislocations wit the burgers-vectors $\boldsymbol{b_1}$ and $\boldsymbol{b_2}$, and (b) possible directions in the (111) plane [11]. 15

2.6 Formation of a $\frac{1}{6}[1\bar{2}1]$ Shockley-partial dislocation in the (111) plane [11]. 15

2.7 (a) Atomic configuration in a twin, and (b) formation of a mechanical twin by slip of four partial dislocations with similar burgers-vector $\mathbf{b_1}$. The bold letters **ABC** indicate the faults in the stacking sequence with respect to the regular fcc stacking sequence in column 1, and the horizontal lines in column 5 represent the twin-boundaries of the mechanical twin [4]. 18

2.8 Schematic arrangement of the grinding vials located on the rotating supporting disk. The green and blue arrows indicate the respective rotation directions. . . . 20

2.9 Grinding ball motion in the vials during milling [35]. 21

2.10 Schematic depiction of (a) the HPT process [38], and (b) the arrangement containing the air-tight encapsulation during compacting [41]. 23

2.11 Depiction of a typical tensile sample. Modified from reference [42]. 24
2.12 Engineering- (solid line) and true (dashed line) stress-strain curves of a ductile material. Modified from reference [42]. 25
2.13 Construction of the yield-point and the mechanical properties that can be conducted from the stress-strain curve: $\sigma_{0.2}$ is the yield-strength, σ_u the ultimate strength, ϵ_u the uniform elongation and ϵ_t the total elongation. The black dot mark the yield point, the vertical line the point of ultimate stress, and the cross the point of failure 26
2.14 XRD-setup: (a) Bragg-Brentano focusing geometry, (b) Diffraction geometry in the sample [12]. 27
2.15 Diffractogram of NaCl powder. The numbers above the peaks represent the respective crystallographic planes [12]. 28
2.16 Explanation of the Full Width at Half Maximum [43]. 29
2.17 (a) interaction volume of the primary electrons with the sample as well as maximum escape depths for the respective signals, and (b) creation of a secondary electron and characteristic X-rays. [45]. 30

3.1 Tensile specimen cut from an HPT-disk: (a) Dimensions of the tensile specimen, (b) specimen after cutting. Dimensions in (a) are given in mm. 34
3.2 Tensile specimen inside the testing module. 35

4.1 Diffractogram of a powderous sample of Cu with 20 wt.% Zn in unmilled condition, and after 1, 2, and 3 hours of ball milling. 38
4.2 Detailed depiction of Figure 4.1. 39
4.3 Change in crystallite size in the powderous test samples with compositions of 10, 20, and 30 wt.% Zn after consecutive milling time. Calculation was done using the FWHM from fitting of the peaks at $2\Theta = 42.4$, 59.4, and 88.9 degrees. . . . 40
4.4 Comparison of samples with 10 wt.% Zn after 10 and 50 revolutions in the HPT: (a) Measured hardness in dependence of the radius. The dashed lines represent the locations that corresponds to the gauge section of the tensile samples. (b) Representative stress-strain curves. The dots mark the yield-strength, the vertical line the uniform elongation, and the crosses the point of failure. 40
4.5 SEM images of samples with 10 wt.% Zn deformed by HPT for (a) 10, and (b) 50 revolutions. The location matches the gauge section of the tensile sample, which is at a radius of 2 mm on the HPT disk. 41
4.6 Measured Hardness values for undeformed HPT samples of pure Cu an 10, 20, and 30 wt.% Zn after 50 revolutions by HPT along the radius. The dashed line at radii of 2 and -2 mm represent the location that corresponds to the gauge section of the tensile samples. 42

4.7 SEM images of samples with 30 wt.% Zn deformed for 50 revolutions by HPT at a radius of (a) 1.5 mm, (b) 2.0 mm, and (c) 2.5 mm. Regardless of radius, this composition shows an inhomogeneous microstructure. 42
4.8 Comparison of stress-strain curves from of the tensile samples fabricated by HPT discs deformed for 50 revolutions: (a) representative curves for tensile samples of pure Cu and CuZn with 10, 20, and 30 wt.% Zn, and stress-strain curves from (b) pure Cu samples, (c) samples with 10 wt.% Zn, and (d) samples with 20 wt.% Zn. The dots mark the yield-strength, the vertical lines the uniform elongation, and the crosses the point of failure. 44
4.9 Grain size distributions and mean grain sizes of (a) pure Cu, samples with (b) 10, and (c) 20 wt.% Zn, and (d) cumulative grain size distribution with critical grain sizes D_C. 46
4.10 TEM images of twins in the deformed tensile samples of (a) pure Cu, and samples with (b) 10, (c) 20 wt.% Zn and (d) overview of several twinned grains in the sample with 10 wt.% Zn. The green lines in (d) mark the recognized twin boundaries used for calculation of the twin densities. 48

A.1 Depiction of an example of the difference between measured and corrected curve. The blue line represents the as measured curve, the orange line the cropped curve, and the green line the linear extrapolation for the cropped part. 58

Chapter 1

Introduction

For several centuries, material scientists have sought to develop materials with increasingly improved physical properties. Especially, the high-tech industry always demands for ”stronger”, ”stiffer” and ”lighter” materials, that can withstand increasingly higher temperatures and harsher environments [1].

One way to achieve this are nano-crystalline (NC) materials, which are defined as polycrystals with grain sizes smaller than 100 nm in at least one dimension [1–6]. In this kind of material, a large portion of the atoms are located at the grain boundaries [1, 7]. Properties of NC materials that are superior to those of their coarse-grained counterparts include, but are not limited to: increased strength/hardness, reduced elastic modulus, higher electrical resistivity, increased specific heat, higher thermal expansion coefficient, lower thermal conductivity, and superior soft magnetic properties [1, 2, 7, 8].

NC materials can be processed by producing a non-equilibrium, high-energy state through melting, evaporation, exposed pressure, stored mechanical energy, irradiation or similar methods. Techniques like rapid solidification or vapor deposition are used to ”freeze” the high-energy state to produce supersaturated solid solutions, metastable crystalline, or quasi-crystalline phases resulting in a NC microstructure [1, 5].

Pure NC Cu produced by severe plastic deformation (SPD) may have a yield-strength six times the yield-strength of coarse-grained Cu [2, 9]. Unfortunately, this impressing increase in strength is accompanied by low ductility due to the lack of work hardening. The reason for this is the inability of NC materials to accumulate and saturate dislocations, caused by the small grain size [3]. This severely restricts the practical application of NC materials [2–4, 8, 10].

Zhao *et al.* [8] showed that dislocation and twin accumulation can be activated in NC-bulk-Cu which was produced by high-pressure torsion (HPT) followed by cold rolling, by lowering the stacking fault energy, the energy necessary to produce stacking faults, of the material through alloying with Zn. This enables mechanical twinning as additional deformation mechanisms, consequently enhancing not only the yield-strength, but also the ductility. Zhao *et al.* concluded that, based on their results, the alloy with optimal stacking fault energy would be 10 wt.% Zn.

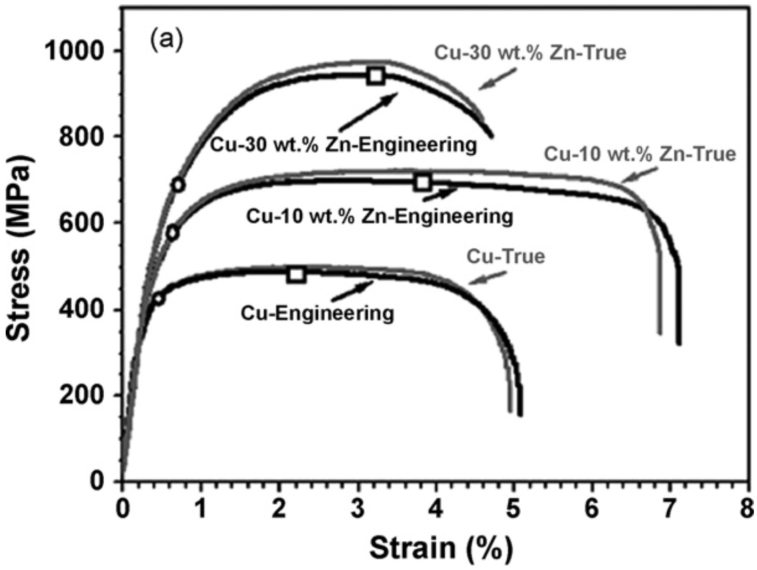

Figure 1.1: Stress-strain curves of tensile experiments conducted by Zhao *et al.* on samples with compositions of pure Cu and CuZn with 10 and 30 wt.% Zn produced by HPT and cold rolling [8].

The goal of this thesis is to apply this knowledge to samples made from powderous raw materials. This way it will be much easier to produce composite samples with varying elements and/or compositions, that can easily be tailored to fit different purposes. The manufacturing process is done in two steps: mechanically alloying/milling of the raw powders, followed by powder consolidation and processing by HPT. From these HPT-disks small tensile samples are cut to determine yield-strength, ultimate strength, uniform elongation, and total elongation in tensile experiments. SEM imaging and Vickers hardness measurement is used to verify the saturation of the microstructure, and TEM to analyze grain size and twin density.

Chapter 2

Theoretical background

2.1 Dislocations

Every crystal contains imperfections, so called defects, which disturb the perfect arrangement of atoms in the crystal, which occur as point-defects (1D), line-defects (2D), and volume-defects (3D). One of the most important defects for metals, which largely governs its ability to deform, are dislocations [11, 12].

For an edge dislocation, the arrangement of the atoms in the crystal can be described by inserting an additional half-plane, see Figure 2.1(a). The two planes adjacent to the inserted plane are separated by one atomic spacing. The largest disturbance of the atoms with respect to their original positions is near the dislocation line, and decreases with increasing distance from it, see line DC in Figure 2.1(a) [11, 12]. Screw dislocations differ in the way that no additional plane is inserted. Instead, the two adjacent planes to the ABCD plane are shifted with respect to each other in the direction of DC, see Figure 2.1(b) [11, 12].

2.1.1 Burgers-vector

Dislocations are defined by the Burgers-vector and -loop, also called Burgers-circuit. The latter describes a closed path going from atom to atom through the crystal. If the same sequence of atoms leads to a different path as in a dislocation-free crystal, then the observed sequence encloses at least one dislocation. The Burgers vector is the vector needed to close the loop, see Figure 2.2 [11–13].

For screw dislocations, the Burgers-vectors are parallel, and for edge dislocations normal to the dislocation line. Dislocations either form closed loops, or branch into one another, as the dislocation lines can only end on the surface of a crystal or at grain-boundaries [11, 12]. Dislocations whose Burgers-vector resembles a lattice vector of the crystal, are called perfect dislocations [11, 13].

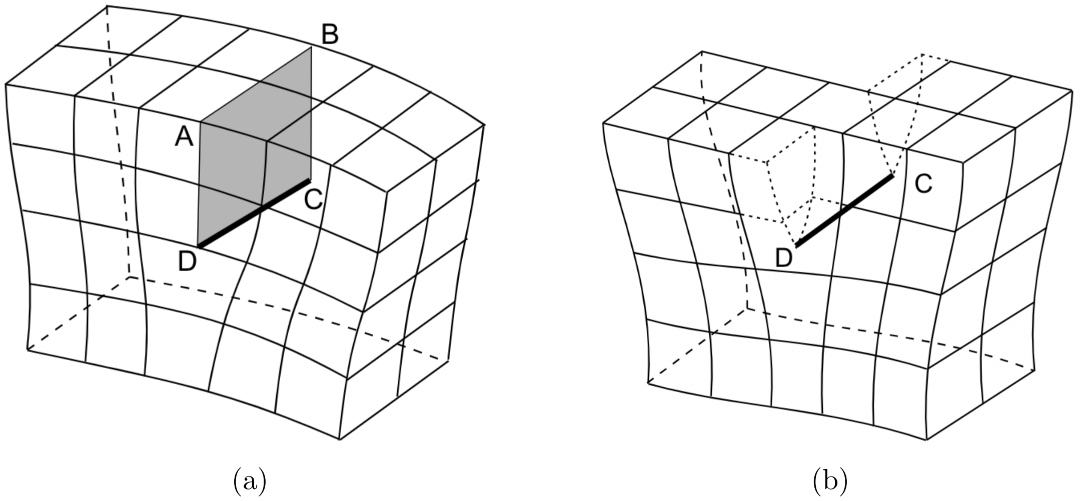

Figure 2.1: Geometry of (a) an edge dislocation, and (b) a screw dislocation. The line DC represents the dislocation line, and ABCD the additional plane of atoms in the edge dislocation [11].

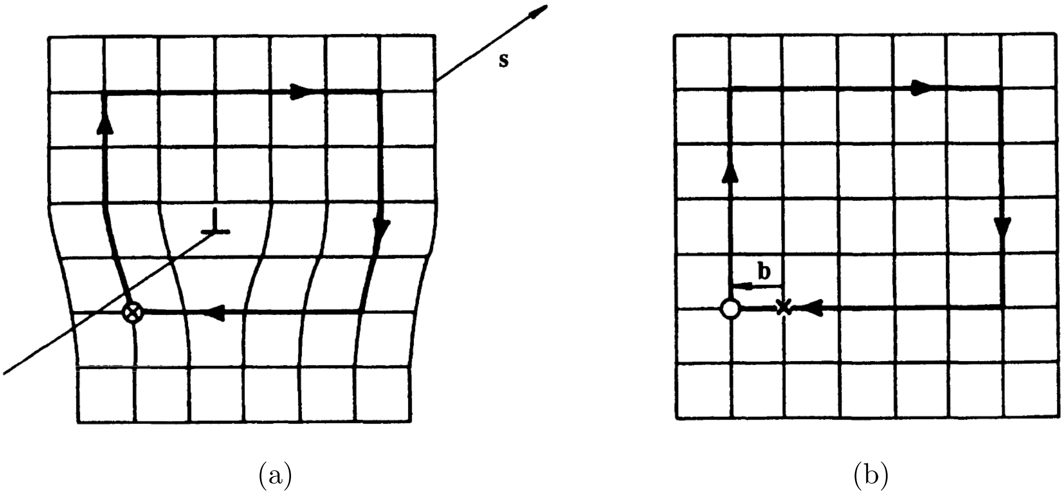

Figure 2.2: Burgers-loop in (a) a crystal that contains a dislocation, and (b) a dislocation-free crystal. The circle and the cross mark start and finish of the Burgers-loop, s indicates the dislocation line, and b the Burgers-vector [12].

2.1.2 Movement of dislocations

There are two main ways in which dislocations may move: glide and climb. Glide is the movement of a dislocation on the plane spanned by its dislocation line and Burgers-vector. Climb, on the other hand, is when the dislocation moves out of its gliding-plane by absorption or emission of point defects [12]. Since high temperatures promotes the movement of point defects through the crystal, climb rarely happens at low temperatures [11].

Consecutive glide of many (edge-) dislocations is called dislocation slip, where one plane of atoms moves across another one. Dislocation slip is the most important manifestation of plastic deformation in metals. The planes on which dislocation slip occurs, are called slip planes. Both, slip planes and slip direction depend on the crystal structure. Usually, slip planes correspond to the planes in the crystal which are most densely packed. Face-centered cubic (fcc) metals, for example, slip across the {111} planes in the ⟨110⟩ directions. The required stress for dislocation slip is far less than what would be expected from moving two sets of atoms across each other. The reason for this is that near the dislocation line, see DC in Figure 2.1, the atoms are not at their ideal position. Thus, only a very small change in atomic spacing is required to move a dislocation across the slip plane, as only one atom at a time has to be moved. Figure 2.3 illustrates this concept through the movement of an atom 1 in respect to the atoms 2 and 3. The needed stress to move a dislocation is called Peierls-Nabarro stress and is several orders of magnitude smaller than the theoretical shear-stress for a perfect crystal [11, 12].

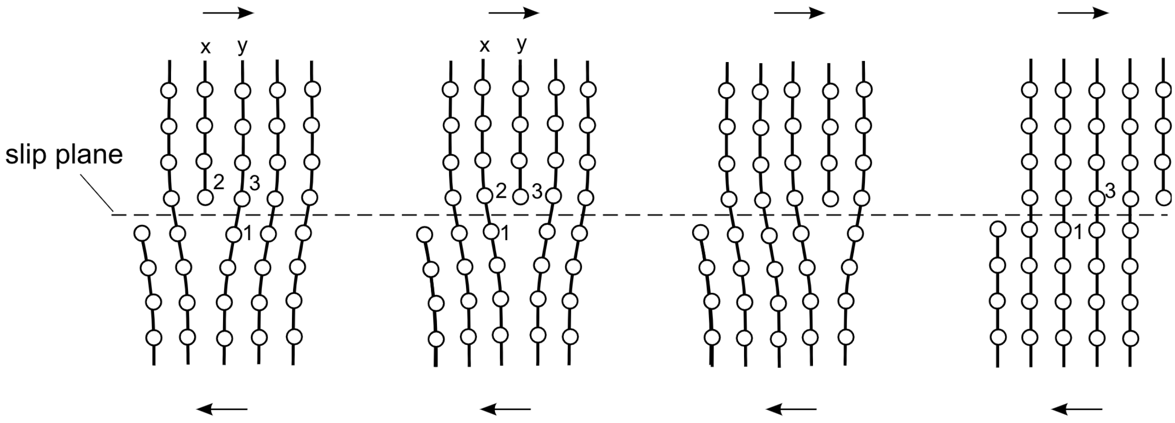

Figure 2.3: Movement of an edge dislocation across a slip plane. The arrows indicate the direction of the applied shear-stress, and the numbers 1 to 3 mark individual atoms [11].

Like edge dislocations, screw dislocations usually move in certain crystallographic planes. In fcc crystals, these are also the {111} type planes. However, it is possible for screw dislocations to switch to another {111} plane, if the other plane contains the direction of the dislocations Burgers-vector. This motion is called cross slip [11, 12]. This allows screw dislocations to bypass obstacles, and can therefore reduce the hardening rate [12]

2.1.3 Work hardening

When (shear-) stress is applied to a crystal, dislocations are created at dislocation sources and glide along their preferred directions, i.e. the directions where the Peierls-Nabarro stress is the smallest. For fcc crystals, these are the ⟨110⟩ directions on the {111} planes. As new dislocations are created, they start to interact with each other and accumulate or pile up at the grain-boundaries, which leads to immobilized dislocations. Further, dislocations exert a back stress on their source, which opposes the external shear stress. The combined stress field from the accumulated dislocations eventually becomes large enough to stop the dislocation source from operating. A strong enough stress field from piled up dislocations can also reach across grain-boundaries and activate secondary dislocation sources in neighboring grains, see Figure 2.4. Dislocations from the secondary sources again glide on their respective preferred directions. Due to different crystal orientation of the neighboring grains, these directions are less favorable for deformation in the direction of the external shear stress. Consequently, the external stress to operate dislocation sources and maintain plastic flow becomes increasingly higher, leading to an increase in strength of the material. This strengthening mechanism caused by deformation is called work- or strain hardening [11, 12].

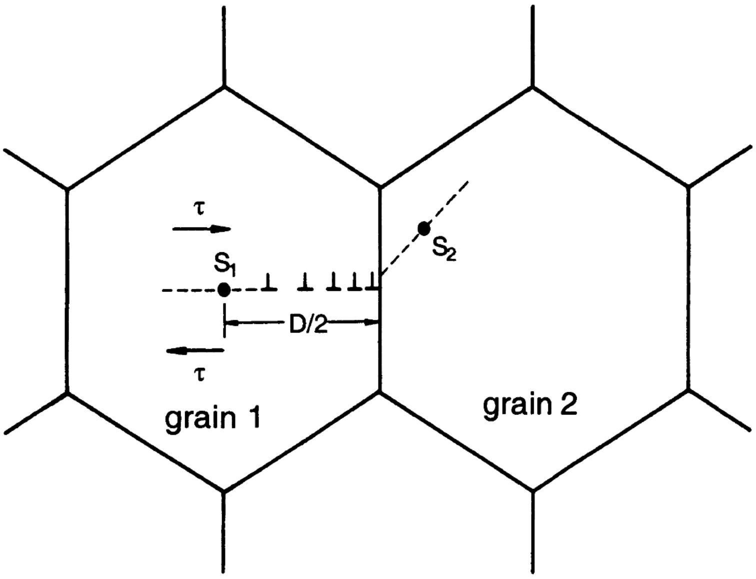

Figure 2.4: Piled up dislocations at the grain-boundary and activation of a secondary dislocation source in the neighboring grain. τ represents the external shear stress, D the grain diameter, S_1 the primary-, and S_2 the secondary dislocation source [12].

2.1.4 Partial dislocations and stacking faults

The line energy E of a dislocation is proportional to the square of its Burgers-vector,

$$E = \frac{1}{2} G b^2, \tag{2.1}$$

with G as the shear-modulus and b as the Burgers-vector [12]. A perfect dislocation with burgers-vector $\boldsymbol{b}$ can therefore reduce its energy by splitting into two partial dislocations $\boldsymbol{b_1}$ and $\boldsymbol{b_2}$, shown in Figure 2.5(a) [11–13]. In contrast to perfect dislocations, glide of such a partial dislocation, whose Burgers-vector does not resemble a lattice-vector, produces a crystal with a stacking fault. The excess energy per unit area to produce a stacking fault is called stacking fault energy γ_{SF} [11, 12]. Whenever a stacking fault ends in a crystal, the border between the perfect crystal and the faulty part therefore represents a partial dislocation, see left side of Figure 2.6 [11].

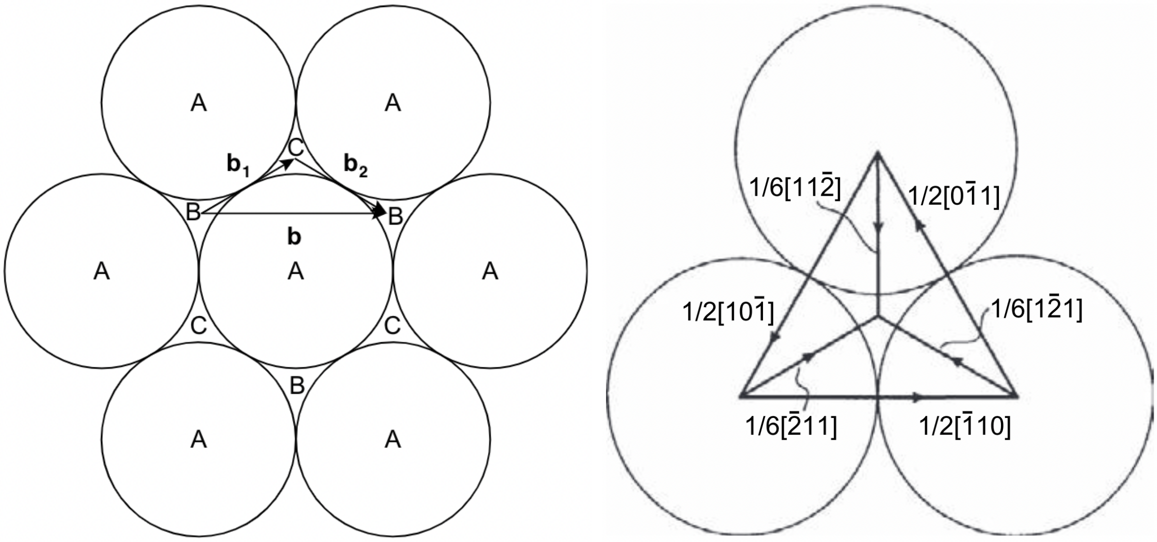
A
A
C
b_1
b_2
B
B
b
A
A
A
C
C
B
A
A
$1/6[11\bar{2}]$
$1/2[0\bar{1}1]$
$1/2[10\bar{1}]$
$1/6[1\bar{2}1]$
$1/6[\bar{2}11]$
$1/2[\bar{1}10]$

(a) (b)

Figure 2.5: Shockley-partial dislocations: (a) Splitting of a perfect dislocation with burgers-vector ***b*** into two partial dislocations wit the burgers-vectors $\boldsymbol{b_1}$ and $\boldsymbol{b_2}$, and (b) possible directions in the (111) plane [11].

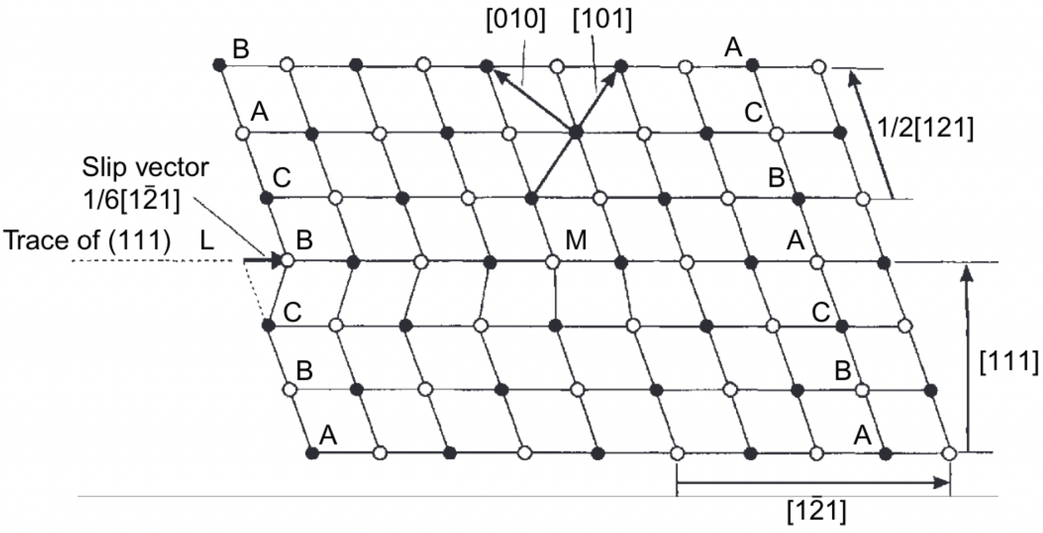
[010]
[101]
B
A
A
C
1/2[121]
Slip vector
$1/6[1\bar{2}1]$
C
B
Trace of (111)
L
B
M
A
C
C
[111]
B
B
A
A
$[1\bar{2}1]$

Figure 2.6: Formation of a $\frac{1}{6}[1\bar{2}1]$ Shockley-partial dislocation in the (111) plane [11].

In an fcc crystal there are three equivalent Shockley-partial dislocations for every of the three {111} slip planes [4, 11]. Figure 2.5(b) shows the six possible directions, as well as the corresponding three Shockley-partial dislocations of the (111)-plane: $\frac{1}{6}[\bar{2}11]$, $\frac{1}{6}[1\bar{2}1]$, and $\frac{1}{6}[11\bar{2}]$ [11].

2.2 Deformation in nano-crystalline materials

In coarse-grained metals and alloys with high ductility, dislocation slip is usually the dominant and most important deformation mechanism [4, 12, 14, 15]. This is especially true at low temperature and low strain rate [4]. Other deformation mechanisms such as grain rotation, grain-boundary sliding and diffusion only get relevant at elevated temperatures, particularly for large grain sizes [4, 12].

However, in contrast to their coarse-grained counterparts, the mechanical properties of NC materials are also governed by additional deformation mechanisms [4]. These include grain-boundary sliding, grain rotation, dislocation emission from grain-boundaries, as well as partial dislocation emission and mechanical twinning [4, 14]. They will be discussed further down below, with mechanical twinning, as the main focus of this thesis, being discussed in more detail. The importance of each of these deformation mechanisms changes with the grain size. Perfect dislocation slip, for example, is the dominant mechanism in fcc metals with medium to high stacking fault energies and grain sizes above 50 nm. In materials with lower stacking fault energy, however, deformation twinning can be activated at lower shear-stresses, allowing the material to deform more easily [4].

The Hall-Petch relationship states that the increase of the yield-strength of a material is indirect proportional to the square-root of the grain size:

$$\sigma = \sigma_0 + \kappa d^{-1/2} \tag{2.2}$$

with σ as the yield-strength, σ_0 a constant, κ the Hall-Petch constant, and d the grain size [4, 6, 7, 12, 14, 16–19]. Similar to work hardening discussed in Section 2.1.3, the reason for this lies in the increased influence of the back stress of dislocations on the dislocation source. With the distances between them being much smaller for small grain sizes [11, 12]. However, recent discoveries suggest that material behavior deviates from the original Hall-Petch relationship for grain sizes below 100 nm [6, 14, 18, 20]. This can be observed through a change of the Hall-Petch constant κ to smaller values when the deformation mechanism changes from dislocation slip to partial dislocation slip. By decreasing the grain size even further to ∼10 - 20 nm, an increasingly higher fraction of atoms are located at grain-boundaries. This results, in contradiction to the Hall-Petch relationship, to a decrease in yield-strength [18, 20]. Much like at high temperatures, grain-boundary sliding and grain rotation become the dominant deformation mechanisms [18]. This effect in NC materials is called reverse Hall-Petch behavior or nanoscale softening [4, 6, 14, 16, 18, 20, 21].

2.2.1 Grain-boundary sliding and grain rotation

As stated above, the relative volume fraction of atoms located near or at the grain-boundaries is exponentially higher in NC materials than in materials with larger grain sizes [1, 14]. Consequently, mechanisms that happen at the grain-boundaries, such as grain-boundary sliding and rotation, will become more dominant in small grains [14, 21]. Both mechanisms can also happen in a coordinated way in form of agglomerates, as the smaller grain sizes make it easier for the grains to align [4, 7, 14]. Grain rotation is believed to happen extremely fast and has been observed to be accompanied by grain growth during deformation [4, 14].

Grain-boundary sliding, as well as grain rotation, are the dominant deformation mechanisms in grains smaller than 10 nm [14]. This observation was proved by molecular dynamics (MD) simulation [4, 14, 20].

2.2.2 Dislocation emission and annihilation at grain-boundaries

Materials with grain sizes from ∼50 - 100 nm largely deform by slip of perfect dislocations [14]. The number of piled up dislocations is a function of the present stress level and the distance from dislocation sources. The number of dislocations present inside the grains therefor decreases for smaller grain sizes, compared to coarse grained materials at the same given stress level [7]. Below a critical grain size, the insides of the grains are basically free of dislocations, as grain-boundaries then act as dislocation sources and sinks, which prevents accumulation of dislocations [3, 4, 7, 14]. The critical grain size where this occurs depends on material properties (e.g. stacking fault energy) and deformation parameters (e.g. temperature, strain rate) [4]. Pile-up and accumulation of dislocations is believed to be the main reason for the work hardening and the Hall-Petch relationship [7]. The smaller number of dislocations and dislocation interactions like pile-ups in NC materials has therefore been identified to be the reason for their lack of work hardening [3, 4, 7].

2.2.3 Partial dislocation emission and mechanical twinning

Another important mechanism in NC materials, especially at low temperatures, is mechanical twinning (also called deformation twinning) [4, 12]. Mechanical twins are produced by shear deformation. The crystal is transformed into a shape with mirror symmetry with respect to the original matrix, while the crystal structure remains the same, see Figure 2.7(a) [12]. Thereby, the crystal is shortened into the direction perpendicular to the shear-stress, while simultaneously being elongated into the shear-stress direction. The respective mirror plane is called twin-boundary [4, 12].

Current understanding is that mechanical twins are formed through the gliding of Shockley-partial dislocations on successive planes [4]. Figure 2.7(b) shows the formation of a mechanical twin by slip of four partial dislocations with similar burgers-vector $\mathbf{b_1}$. The first column shows a regular fcc stacking sequence ABCABC. After the slip of the first partial dislocation, a stacking fault is produced, which is represented by the bold letter **C** in column 2. Slip of further partial dislocations gradually adds stacking faults until a four layered twin is produced in column 5, with the horizontal lines representing the twin-boundaries [4]. The direction of the burgers-vector $\mathbf{b_1}$ corresponds to the same direction depicted in Figure 2.5(a).

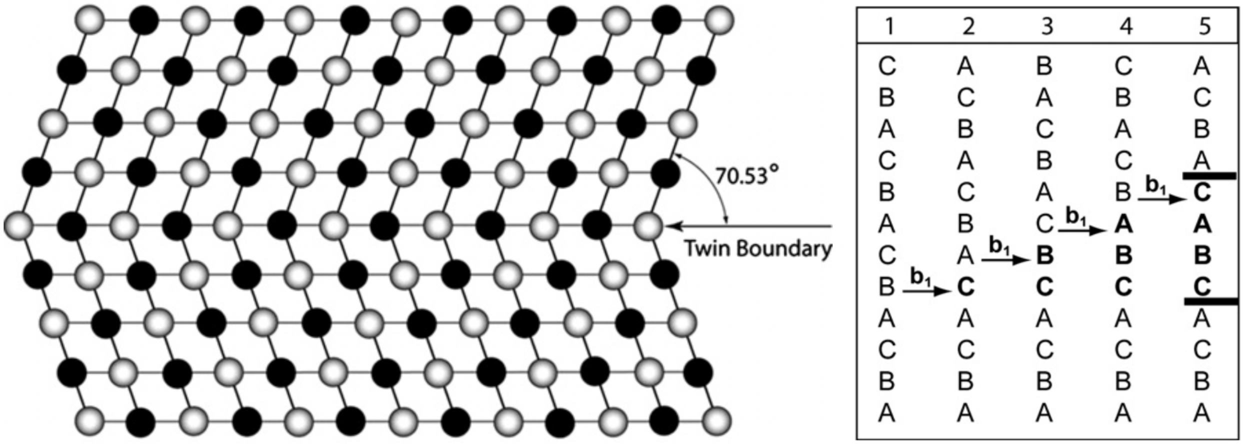

1	2	3	4	5
C	A	B	C	A
B	C	A	B	C
A	B	C	A	B
C	A	B	C	A
B	C	A	B	$\xrightarrow{b_1}$ **C**
A	B	C	$\xrightarrow{b_1}$ **A**	**A**
C	A	$\xrightarrow{b_1}$ **B**	**B**	**B**
B	$\xrightarrow{b_1}$ **C**	**C**	**C**	**C**
A	A	A	A	A
C	C	C	C	C
B	B	B	B	B
A	A	A	A	A

(a) (b)

Figure 2.7: (a) Atomic configuration in a twin, and (b) formation of a mechanical twin by slip of four partial dislocations with similar burgers-vector $\mathbf{b_1}$. The bold letters **ABC** indicate the faults in the stacking sequence with respect to the regular fcc stacking sequence in column 1, and the horizontal lines in column 5 represent the twin-boundaries of the mechanical twin [4].

As mechanical twins are built from stacking faults, the likelihood of fcc materials, such as Cu, to deform by mechanical twinning depends largely on the stacking fault energy. Lower values encourage deformation by twinning [4, 7, 12, 19, 22, 23]. However, twinning can be promoted by high strain rates and low temperatures [4, 23, 24].

Fcc materials that deform by twinning also exhibit a higher work hardening rate. The reason for this is that twin-boundaries act as barriers for the slip of perfect dislocations [4, 9, 12, 23]. Thus, while the crystal can deforms by twinning, the increasing number of twin-boundaries restrict the movement of perfect dislocations, increasing the strength of the crystal. Perfect dislocation-slip (and therefore dislocation accumulation/pile-up) and mechanical twinning can happen simultaneously, which consequently allows simultaneous increase of strength and ductility [4, 9].

Molecular dynamics (MD) simulations suggest that emission of partial dislocations and mechanical twinning are the dominant deformation mechanism at grain sizes ~ 10 - $50\,\mathrm{nm}$ [14]. The critical grain size D_C that governs the transition of perfect dislocation slip to mechanical twinning as the dominant deformation mechanism in NC metals can be calculated as:

$$D_C = \frac{2\alpha G(b_N - b_P)b_P}{\gamma_{SF}} \tag{2.3}$$

With α representing the kind of dislocation (0.5 for edge- and 1.5 for screw dislocations), b_N the magnitude of the perfect-, and b_P the magnitude of the partial dislocation [25]. Using the possible directions in the (111) plane from Figure 2.5(b), the magnitude of perfect- and partial dislocations can be calculated using:

$$b_N = \frac{a}{2}\sqrt{h^2 + k^2 + l^2} \tag{2.4}$$

and

$$b_P = \frac{a}{6}\sqrt{h^2 + k^2 + l^2}. \tag{2.5}$$

With a as the lattice constant and h, k, l as the Miller indices of the crystallographic directions [11, 26]. Table 2.1 shows the reference values used for the calculation, as well as the calculated values for the critical grain sizes. The mean value of $\alpha = 1$ was used for the calculation.

Table 2.1: Reference values for lattice constant a [27], stacking fault energy γ_{SF} [19, 28], and shear modulus G [29], as well as the calculated values for the critical grain size D_C.

samples	**Cu100**	**Cu90Zn10**	**Cu80Zn20**	**Cu70Zn30**
a / [Å]	3.615	3.64	3.65	3.67
γ_{SF} / [mJ/m^2]	45	35	18	14
G / [GPa]	46	43.6	40.3	37
D_C / [nm]	32	40	73	87

Deformation by mechanical twinning in fcc metals first becomes easier with decreasing grain size, then more difficult [23, 28, 30, 31]. In NC materials it becomes increasingly hard for dislocations to form inside the grains. Thus, dislocations have to be emitted from grain boundaries. For such small grains, however, it is much easier to emit partial dislocations than perfect dislocations [23, 31]. With further decreasing grain size twinning becomes more difficult due to an effect called de-twinning, which is believed to be caused by the interaction of partial dislocations with twin boundaries [32]. Due to this "normal" and inverse grain size effect, an optimal grain size or grain size range for mechanical twinning has been reported to be 46 nm [23, 30] for pure Cu, 44 nm for Cu with 10 wt.% Zn, and 144 nm for Cu with 30 wt.% Zn [28]. Experimental observations seem to back the qualitative trend of an increase in optimal grain size with increasing Zn fraction, and therefore decreasing stacking fault energy γ_{SF}. The observed effect is, however, much weaker than predicted by calculations, with an optimal grain size of 35 nm and 54 nm for compositions with 10 and 30 wt.% Zn, respectively [28].

These optimal grain sizes, however, do not match with the previously calculated critical grain sizes. The reason for this may come from inconsistent values for the reported stacking fault energies for CuZn-alloys, that are used for the calculations [8, 19, 28, 29, 33]. Further, the model of the critical grain size bears several simplifications, as is does not account for elastic anisotropy, the small Peierls-Nabarro stress, localized stress concentrations, and the grain-boundary interaction of dislocations [25]. The general trend, however, is consistent with experiments, and suggests that both, critical and optimal grain size, lie in the range of 30 to 90 nm, for the investigated compositions [25, 28].

2.3 Ball milling

Ball milling is used for mechanical alloying and/or mechanical milling of powders [34–36]. It consists of several vials that are arranged on a rotating support disc. Vials and support disc rotate in opposite directions around their own respective axes, as depicted in Figure 2.8 [35].

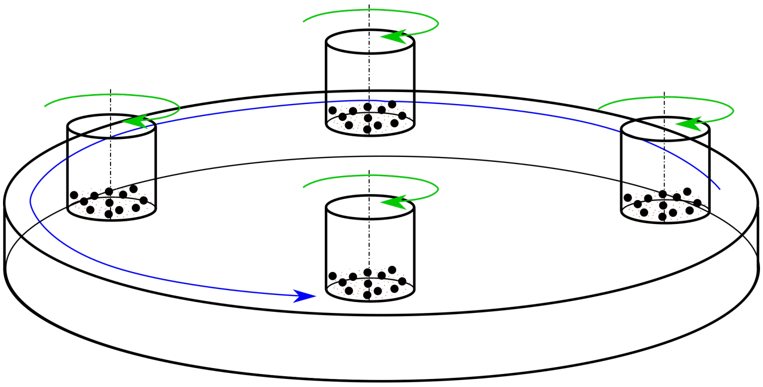

Figure 2.8: Schematic arrangement of the grinding vials located on the rotating supporting disk. The green and blue arrows indicate the respective rotation directions.

During milling the vials are filled with several grams of powder and grinding balls. Both, the vials and the grinding balls, are made of gate, siliconnitride, sintered corundum, zirconia, Cr steel, Cr-Ni steel, tungsten carbide or plastic polyamide [35]. As raw materials powders of different grain sizes (between 1-200 μm) can be used. The grain size is not critical as long as it is smaller than the grinding ball size [35].

The rotation in opposite directions of vials and support disc leads to a constant change in direction of the centrifugal force which acts on the grinding balls. This causes the grinding balls to first run down the inner wall of the vials and grinding the powder (friction effect), followed by lifting off and hitting the opposite side of the vial (impact effect), see Figure 2.9. Because of this the powder is mechanically alloyed and ground down through repeated cold welding, fracturing and rewelding of the powder particles until a steady state is reached [35, 36].

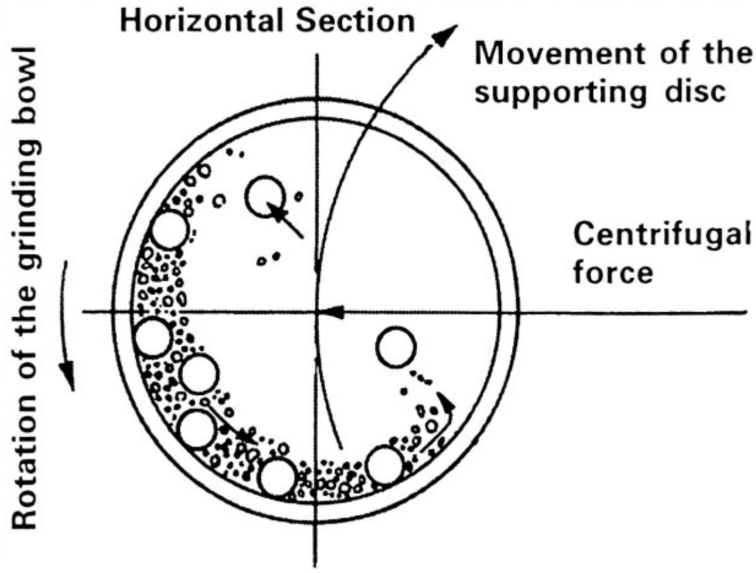
Horizontal Section
Movement of the supporting disc
Centrifugal force
Rotation of the grinding bowl

Figure 2.9: Grinding ball motion in the vials during milling [35].

Several process parameters such as milling speed, milling time, size and size distribution of the grinding balls, ball to powder ratio, temperature and milling atmosphere determine the final form of the milled powder [35]. Additional, the contamination of the powder from the vial can also be of concern. The level of contamination depends on the milling conditions, such as milling time, milling speed, material composition etc.. Ways to minimize contamination are: using the same materials for powder and vial/grinding balls, coated vials/grinding balls, usage of high purity metals, and short milling times [35, 36]. As a general rule, the material of the vial and grinding balls should be stronger/harder than the milled powder [35].

Due to the reactive nature of most powders, milling is performed under either inert gas atmosphere (usually argon) or vacuum [35, 36]. Alternatively, a liquid process control agent (PCA) or very low temperatures (”cryomilling”) can be used to minimize the effect of cold welding during milling. This is especially used for ductile materials. Nevertheless, the use of liquid PCA leads to increased contamination of the powder [35].

2.4 High-pressure torsion

High-pressure torsion (HPT) is among Equal Channel Angular Pressing and Accumulative Roll Bonding one of the three most prominent methods of SPD [37]. Due to high achievable strains SPD can produce ultra-fine grained and NC microstructures [37–39]. One benefit of HPT over other SPD techniques is the superimposed hydrostatic pressure, which allows even higher strains and therefore finer microstructures as well as processing of brittle or high-strength materials, which can be very difficult or impossible to deform by other SPD techniques [37–39]. Additional applications for HPT include powder consolidation and production of supersaturated solid solutions of usually immiscible elements [37, 38, 40].

Today's machines use a so called quasi-constrained HPT setup where a disc shaped sample is placed between two anvils which are rotated with respect to each other under high pressure, see Figure 2.10(a). Sample diameters between 6 mm and 60 mm are possible. Both anvils have a small cylindrical cavity which resembles the diameter of the sample. The combined depth of these cavities has to be less than the sample thickness [37–39]. Under the assumption that no decrease in sample thickness occurs, the applied shear strain γ can be calculated as:

$$\gamma = \frac{2\pi r}{t} n \tag{2.6}$$

with r as the radius, t as the sample thickness and n as the number of revolutions. The equivalent plastic strain ε, resembling a von Mises equivalent strain, can then be calculated as follows [37–39],

$$\varepsilon = \frac{\gamma}{\sqrt{3}}. \tag{2.7}$$

In theory, the shear strain should increase linearly from the center to the edge of the sample, resulting in finer grains at higher radii. With increasing number of revolutions, the zone of finer grained and homogenous microstructure should increases towards smaller radii until saturation is reached, with the center of the sample remaining undeformed. However, at the sample center there still will be deformation due to not perfectly aligned rotation axis of the two anvils [37, 38].

For the fabrication of the disk shaped samples, powdery or granular raw material is used, which is then compacted inside a Cu ring and between the anvils using high pressure and low strains. Powders are very sensitive to oxidation, thus, the whole compacting process is done within protective gas atmosphere, in this case argon. This is done using an air-tight encapsulation, which covers the parts of the anvils where the sample is located. The arrangement during compaction of the powder is depicted in Figure 2.10(b). Anvils, encapsulation, and powder are assembled inside a glove-box under protective gas atmosphere, and are then placed inside the HPT-machine.

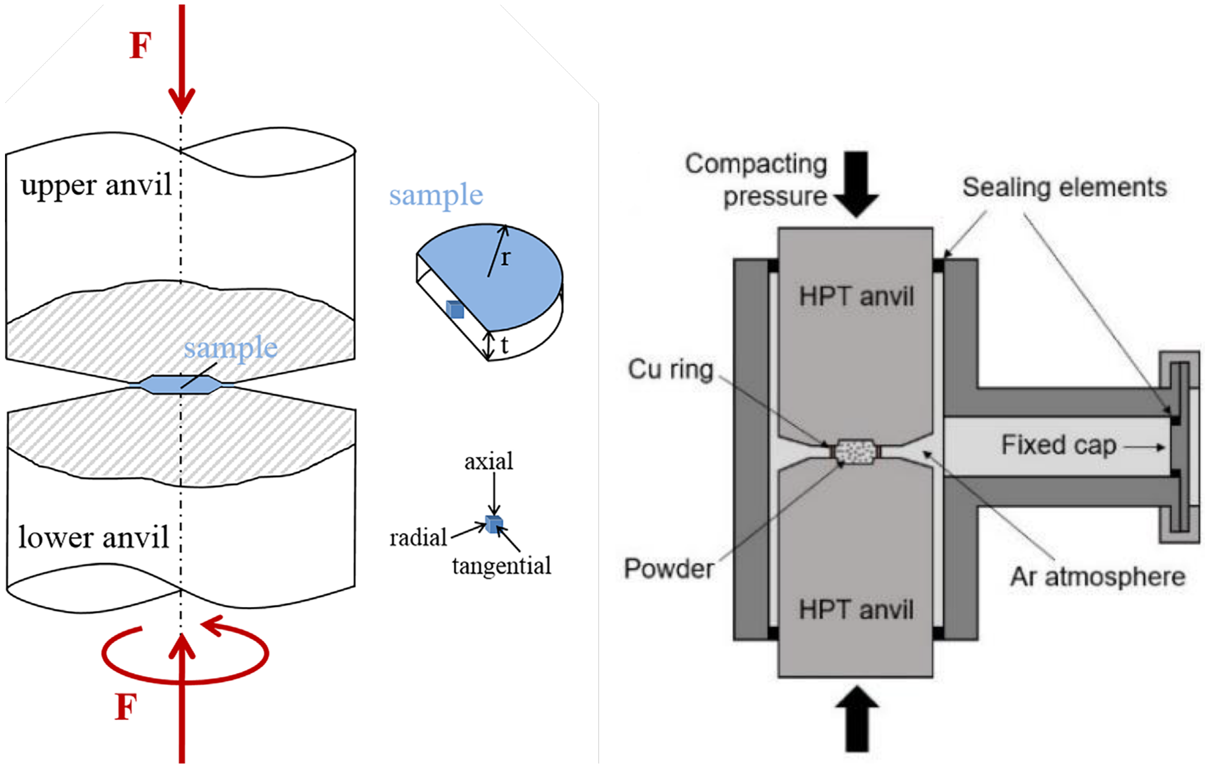
F
upper anvil
sample
sample
r
t
lower anvil
axial
radial
tangential
F
Compacting pressure
Sealing elements
HPT anvil
Cu ring
Fixed cap
Powder
Ar atmosphere
HPT anvil

(a) (b)

Figure 2.10: Schematic depiction of (a) the HPT process [38], and (b) the arrangement containing the air-tight encapsulation during compacting [41].

To increase friction between the compacted samples and the cavities of the anvils during deformation, the cavities are sandblasted. This prevents "slipping" of the sample and enables very high friction forces during the deformation process [37]. Deformation of the samples can also be performed at elevated temperatures by heating the two anvils with an induction coil, or at reduced temperatures where the anvils are cooled by a coolant (e.g. liquid nitrogen). Deformation temperature significantly affects saturation grain size and the necessary strain to achieve saturation. Higher temperatures lead to a bigger saturation grain size and lower saturation strain [39].

2.5 Tensile testing

Tensile testing is used to obtain material properties. During the tensile experiment the tensile sample is subjected to uniaxial tension. The most common testing devices are so called universal tester, which are also capable of conducting bending and compression tests. A typical tensile sample can be seen in Figure 2.11. The most important part of the sample is the gauge section. Its cross section is smaller compared to the shoulders to localize deformation and fracture in this area during testing. The main reason for tensile testing is the recording of a stress-strain curve [42].

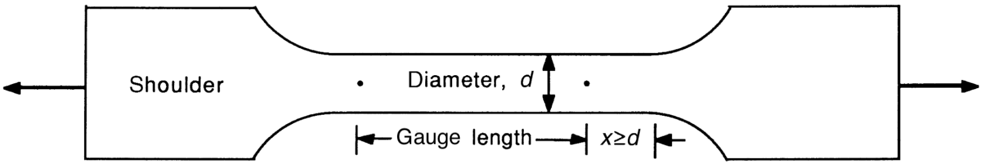

Figure 2.11: Depiction of a typical tensile sample. Modified from reference [42].

During testing the sample is subjected to tension with a constant strain rate by the testing machine. The applied force is measured using a load cell as a function of change in length of the gauge section [12, 42]. Common ways to measure the length change of the gauge section are extensiometers, strain gauges, laser interferometers or video extensiometers. Using the obtained data from the experiment, engineering stress σ and -strain ϵ can be calculated as:

$$\sigma = \frac{F}{A_0}, \tag{2.8}$$

and

$$\epsilon = \frac{\Delta L}{L_0} \tag{2.9}$$

respectively. With F as the applied force, A_0 as the initial cross section area of the gauge section, ΔL as the change in length-, and L_0 as initial length of the gauge section [12, 42]. Beside the material properties there are other factors that influence the shape of the stress-strain curve, e.g. ambient temperature and strain rate. The solid line in Figure 2.12 shows a typical engineering stress-strain curve of a ductile material [42].

At the beginning of deformation the material is subjected to small stresses, that only stretch the atomic bonds. When the stress is removed, the crystal returns to its original shape. This is called elastic deformation [12, 42]. At higher stresses the crystal begins to deform by sliding of atomic planes over each other, see Section 2.1.2. In this case the material does not return to its original shape, although it will recover back for the elastic part of the deformation. This kind of deformation is called plastic deformation, and the remaining strain is called plastic strain. [42].

Most materials show elastic behavior at the beginning of deformation, which manifests in a linear part at the start of the stress-strain curve. According to Hook's law:

$$E = \frac{\sigma}{\epsilon} \tag{2.10}$$

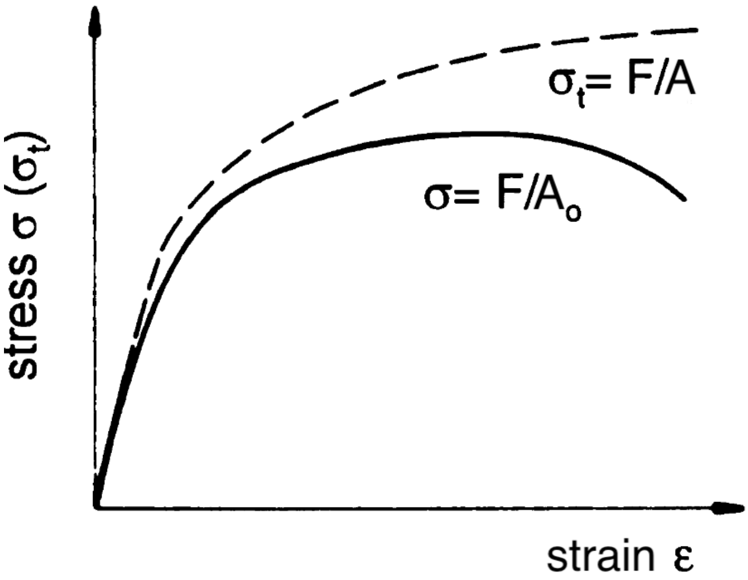

Figure 2.12: Engineering- (solid line) and true (dashed line) stress-strain curves of a ductile material. Modified from reference [42].

The Young's modulus E is the slope of this linear elastic part [12, 42]. To measure the exact point where the curve deviates from the linear behavior is difficult, as it is strongly depends on the sensitivity of the stress and strain measurement. To ensure reproducibility a so called yield-point is defined as an offset for plastic deformation. It can be constructed by fitting a straight line in the elastic part shifting it to an elongation of 0.2%, see Figure 2.13. The stress that is associated with the yield point is called yield-strength $\sigma_{0.2}$ of the material [12, 42].

σ_u is called ultimate stress (sometimes tensile stress or ultimate tensile stress) and corresponds to the point of highest engineering stress. The elongation related to the ultimate stress is called uniform elongation and is obtained by shift parallel the fitted line of the elastic part to the ultimate stress point. The intersection of this line with the x-axis represents the uniform elongation. At the point of the ultimate stress, the deformation in the gauge section localizes and the sample starts to neck. This leads to a reduction in cross section of the gauge section and therefore a decrease in the engineering stress. Up to this point the sample is work hardened, continuously increasing the necessary stress for further elongation. [12, 42]. At ultimate strength, the physical hardening is overtaken by the geometrical softening that results from the necking [12].

The elongation corresponding to the point of failure is called total elongation ϵ_t. Some materials fracture before necking or even before the yield point. In this case the stress at the point of failure is considered the ultimate strength. Thus, it is possible for a very brittle material to have an ultimate strength, but no yield-strength [42].

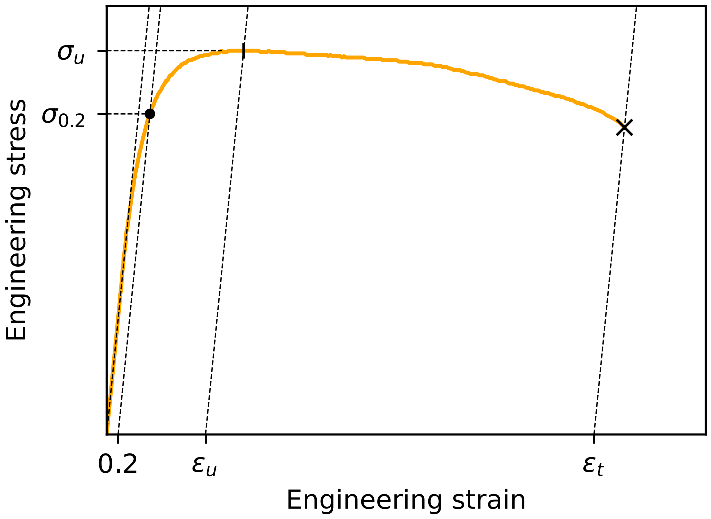

Figure 2.13: Construction of the yield-point and the mechanical properties that can be conducted from the stress-strain curve: $\sigma_{0.2}$ is the yield-strength, σ_u the ultimate strength, ϵ_u the uniform elongation and ϵ_t the total elongation. The black dot mark the yield point, the vertical line the point of ultimate stress, and the cross the point of failure

As the engineering strain is calculated with respect to the initial cross section of the gauge section in mind, it does not accurately depict the deformation after necking sets in. A so called true stress strain curve can therefore be plotted by calculation true stress σ_t and true strain ϵ_t using:

$$\sigma_t = \frac{F}{A}, \tag{2.11}$$

and

$$\epsilon_t = \ln\frac{L}{L_0}. \tag{2.12}$$

With A as the actual current cross section area of the gauge section and L as the current length of the gauge section [12, 42]. When necking sets in, however, the current cross section area has to be measured directly instead of being derived from elongation measurement. The dashed line in Figure 2.12 shows a true stress-strain curve [42].

2.6 X-ray diffraction

X-ray diffraction (XRD) occurs when an electromagnetic wave interacts with a periodic structure (e.g. periodically arranged atoms) [43]. Wavelength of x-rays used in diffraction range from 0.5 - 2.5 Å. This is necessary in order to analyze structures of atomic scale, with the interatomic distances being 1 - 10 Å [43]. Applications in material science include phase analysis, as well as investigations of residual stress/strain, texture, and line broadening analysis [44]. The x-rays needed for measurement are produced using x-ray tubes or synchrotrons [12, 44].

For the measurement of powder or polycrystalline samples with random orientation, powder diffraction is performed, which necessitates monochromatic x-rays. To achieve this, optical filters and monochromators are used to cancel out the continuous part of the spectrum. This way, only the characteristic wavelength of the target material used remains in the x-ray tube [12, 43, 44]. For powder diffraction, usually a Bragg-Brentano focusing geometry is used for measurement, see Figure 2.14(a) [43]. The monochromatic x-rays are focused on the sample, while the detector moves along a specific angle on a goniometer arc, as can be seen in Figure 2.14(a) [12, 43].

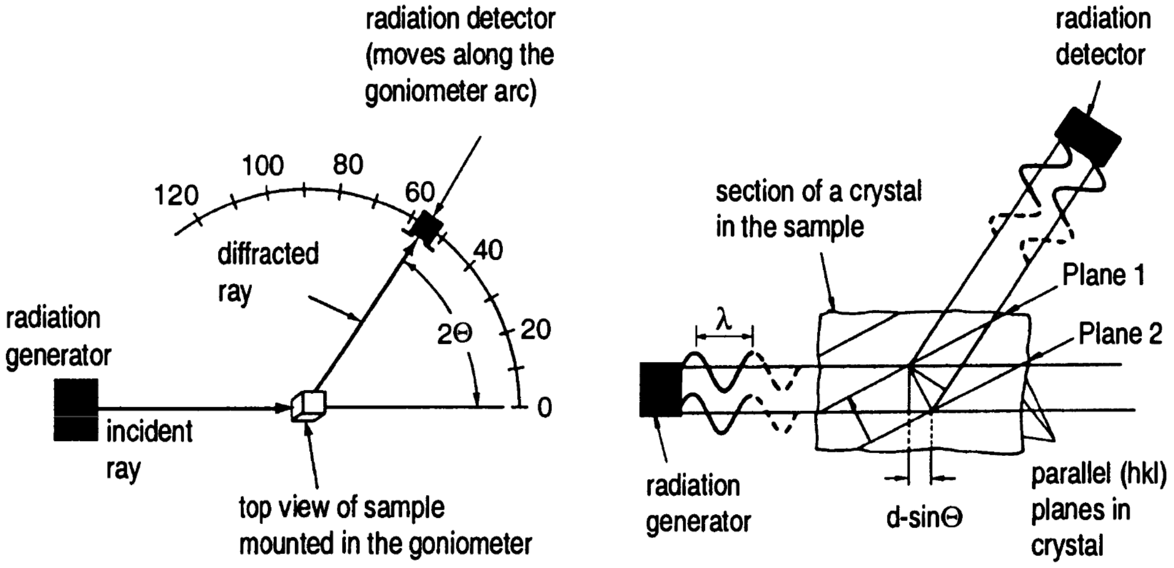
radiation detector (moves along the goniometer arc)
120
100
80
60
40
20
0
diffracted ray
2Θ
radiation generator
incident ray
top view of sample mounted in the goniometer
radiation detector
section of a crystal in the sample
Plane 1
Plane 2
λ
radiation generator
d-sinΘ
parallel (hkl) planes in crystal

(a) (b)

Figure 2.14: XRD-setup: (a) Bragg-Brentano focusing geometry, (b) Diffraction geometry in the sample [12].

The distances from generator and detector to the sample are constant during measurement. Constructive interference occurs if a lattice plane in the sample satisfies the Bragg equation,

$$n\lambda = 2d \cdot sin\Theta, \tag{2.13}$$

with n as the order of interference maxima, λ as the wavelength, d as the lattice plane spacing, and Θ as the angle between incident/diffracted ray and the lattice plane [12, 43, 44].

Plottings of these intensities over 2Θ are called diffractogram. It consists of a background part, as well as characteristic peaks, which correspond to the different lattice planes hkl of the crystallites in the sample [12]. Figure 2.15 shows the diffractorgram of NaCl powder.

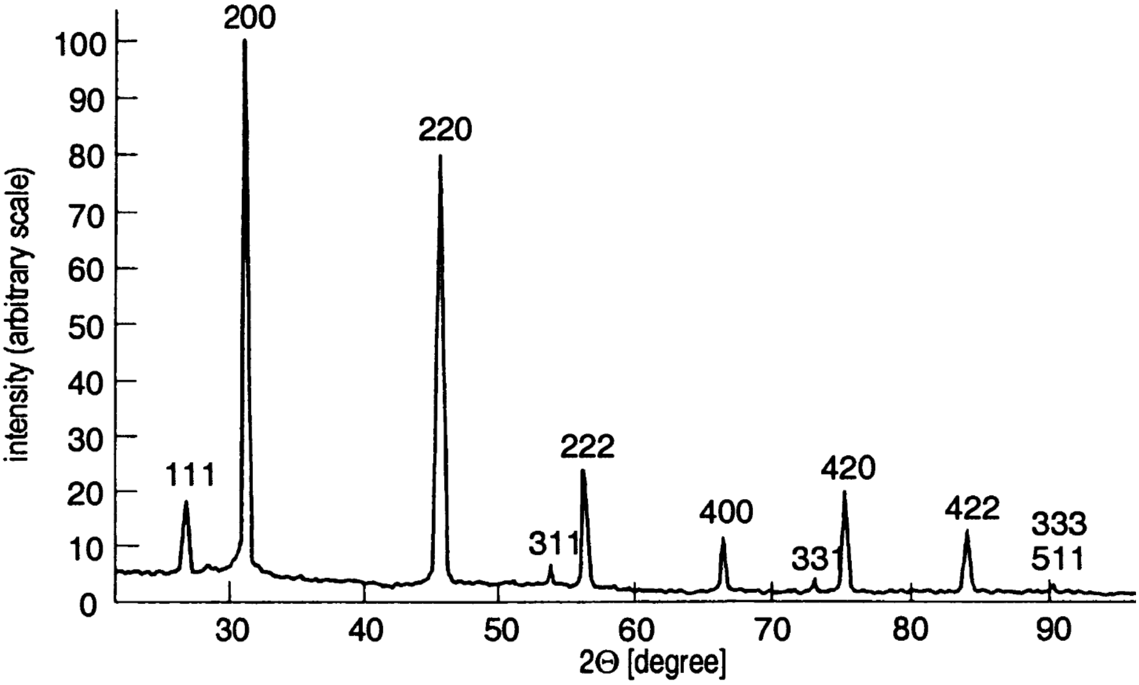

Figure 2.15: Diffractogram of NaCl powder. The numbers above the peaks represent the respective crystallographic planes [12].

However, it has to be kept in mind that not every crystallographic plane from every crystal structure produces a reflection, even if Brags's equation is satisfied. Fcc crystals, for example, will only produce reflections, if the Miller indices of the lattice planes hkl are either all even or all odd [12]. If the composition of the investigated sample is known, databases can be used to match the different peaks of the diffractogram to the respective lattice planes. The intensity peaks visible in the diffractogram can be used to determine the relative amount of the different phases, corresponding to the lattice planes, present in the sample [12, 43].

The peak width on the other hand gives information about the size of the crystallites. In theory, a perfect single crystal would have a very narrow, almost line shaped peak. In an actual real world sample, there are several crystallites with different imperfections present. This leads to a certain distribution of diffracted intensities, resulting in broader peaks [43]. The Full Width at Half Maximum (FWHM) can be used to determine the size of the crystallites in powderous samples using the Sherrer equation [43],

$$FWHM \approx \Theta_2 - \Theta_1 = \frac{0.9\lambda}{D \cdot cos\Theta} \tag{2.14}$$

with D as the crystallite size [43, 44]. Usually the FWHM is approximately half of the difference between $2\Theta_2$ and $2\Theta_1$, see Figure 2.16 [43].

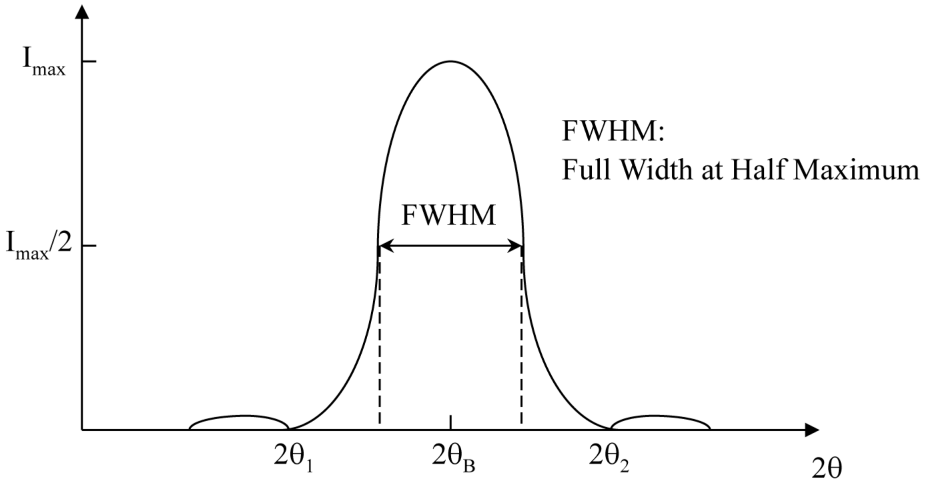

Figure 2.16: Explanation of the Full Width at Half Maximum [43].

It should be kept in mind, that the Sherrer equation is only applicable for crystallites smaller than 0.2 µm and will predict the crystallite size rather on the lower bound [43].

2.7 Scanning electron microscopy

Scanning electron microscopes (SEM) use electrons for imaging. Depending on the voltage used to accelerate the electrons, wavelengths of several pm are possible, which results in a lateral resolution of only a couple of nm. Unlike other microscopes, SEMs have a very high magnification range of 10 to 500,000. Because of their negative charge electrons interact strongly with atoms, leading to a wide range of emissions that can be detected [45].

In SEM electrons are emitted by an electron gun, accelerated by an anode and focused on the sample using multiple electromagnetic lenses. The focused electron beam then sequentially scans the surface of the specimen. A variety of detectors can be used to detect the emitted signals. During operation the sample is located on an motorized sample stage. Inside the SEM chamber the pressure is low vacuum to prevent interactions from the electrons with gas molecules. Typical SEM pressures range from 0.1 to 10^{-4} Pa. The accelerating voltage for the electrons usually ranges from 1 to 30 kV [45].

Electrons can interact either elastically or inelastically with matter. Elastic scattering of electrons can be used to analyze the crystal structure. In contrast to this, inelastic scattering is accompanied by energy loss during interaction. Figure 2.17(a) shows the volume in which the electrons interact with the sample, which is called interaction volume[45].

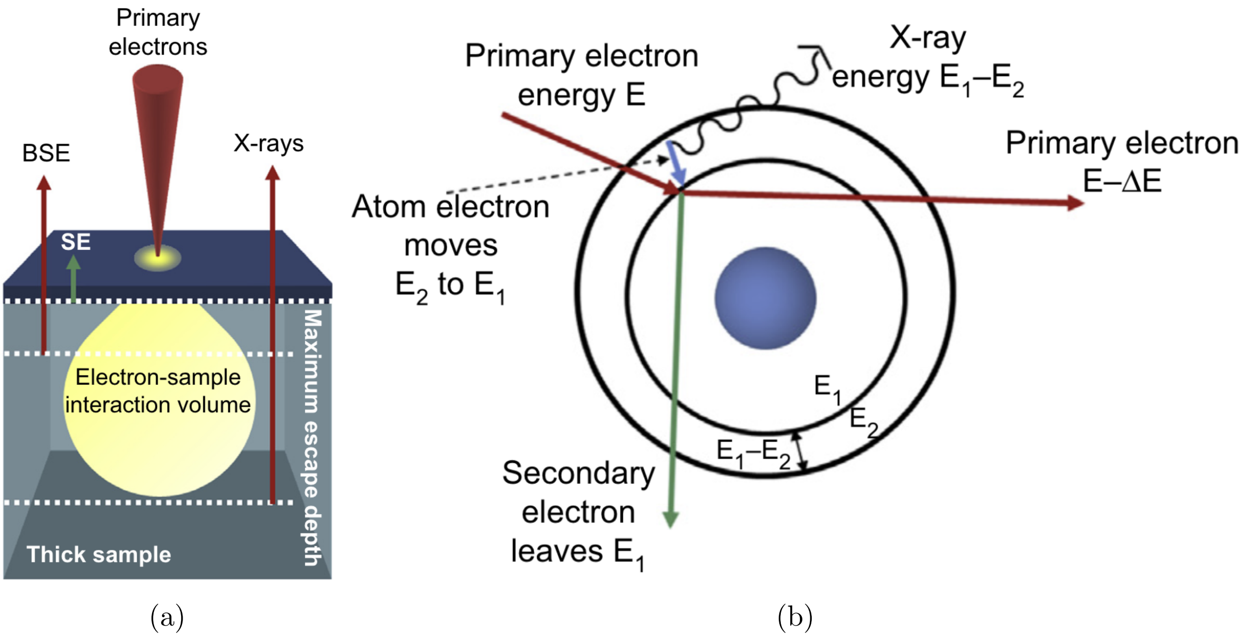
Primary electrons
BSE
X-rays
SE
Electron-sample interaction volume
Maximum escape depth
Thick sample
Primary electron energy E
X-ray energy E1–E2
Primary electron E–ΔE
Atom electron moves E2 to E1
E1
E2
E1–E2
Secondary electron leaves E1
(a)
(b)

Figure 2.17: (a) interaction volume of the primary electrons with the sample as well as maximum escape depths for the respective signals, and (b) creation of a secondary electron and characteristic X-rays. [45].

The main emissions that can be detected from the interaction of the primary electrons with the sample are backscattered electrons (BSE), secondary electrons (SE), and X-rays. Inelastic scattering of the signals govern from which depth, called maximum escape depth, they can escape from inside the sample [45].

BSEs are electrons from the incident beam that are scattered in such an angle that they emerge back out of the sample. They are created by the interaction of the electrons with the nuclei of the atoms in the sample. The number of generated BSEs is proportional to the atomic number Z of the nuclei. Thus, heavier elements cause a brighter signal compared to lighter elements. BSE detectors are therefore well suited to distinguish different phases from each other. They are usually mounted right above the sample inside the SEM chamber. The maximum escape depth of BSEs depends on the energy of the incident primary electrons. [45].

SEs are electrons that are generated when primary electrons knock electrons in the sample atoms out of their shell, as illustrated in Figure 2.17(b). Most generated SEs are absorbed by inelastic scattering by the sample. Only SEs close to the surface have sufficient energy to escape the sample. The angle between the incident beam and the surface affects how many SEs are emitted. The maximum escape depth for SEs is 20 nm. A heavily tilted beam compared to the surface leads to a big interaction area and therefore a high number of emitted SEs. Thus, SE detectors are very convenient for analyzing the topography of the sample surface, as sharp edges will appear brighter in the SEM image [45].

X-rays are created by two effects in the SEM. Bremsstrahlung is generated when a primary electron is slowed down by interaction with a specimen atom. The difference in energy is emitted in form of X-rays. Characteristic X-rays on the other hand are produced when a SE is created and an electron that sits at a higher energy position (E_2) transitions to the lower energy position (E_1) that was formerly occupied by the SE, see Figure 2.17(b). The energy difference of the transfer is again emitted in form of X-rays. This time with characteristic wavelength for the respective element. Characteristic X-rays can therefore be used for chemical analysis. X-rays are capable of escaping from everywhere in the interaction volume [45].

Chapter 3

Material synthesis and characterization

3.1 Sample preparation

Commercial available Cu (spherical, 170+400 mesh, 99.9%, O < 1000 ppm) and Zn (Alfa Aesar, -100 mesh, 99.9%) powders were used as raw materials for the samples and were mixed in the compositions of 10, 20 and 30 wt.% Zn, respectively. To determine the optimal parameters for milling duration and number of revolutions for HPT deformation, a parameterstudy was conducted, see section 4.1.

The mixed powders were milled using a planetary Ball Mill (Retsch PM400) for mechanical alloying and homogenization. For every of the three compositions, 15 g of powder was paired with 150 g of stainless steel balls with a diameter of 5 mm and milled at 200 rpm inside a stainless steel vial. During the parameterstudy, test powders with compositions of Cu with 10 and 20 wt.% Zn were milled for 3 hours. The composition of 30 wt.% Zn was milled for 2 hours, as at this time it was already apparent that 2 hours of milling is sufficient to reach saturation, regardless of composition. The powders that where used to manufacture the tensile samples were milled for a total of 1.5 hours, as it was found by XRD measurements to be sufficient to alloy the elements. Milling was performed for 5 minutes at a time, followed by a 5 minute break to allow vial, powder and grinding balls to cool down. This was done to minimize the possible influence of heat generation during the milling process. To prevent oxidation, mixing of the powders, as well as loading and unloading of the vial was performed under protective argon gas atmosphere inside a glove box. For the parameterstudy, XRD data of the unmilled and milled test powders was recorded with a Bruker D2 Phaser using Co-K_α-radiation and a 1 mm slit. Reference data for the peak positions of Cu, Zn, and CuZn for the XRD diffractograms were taken from the Crystallography Open Database (COD) [46]. Fitting of the XRD data for FWHM evaluation was done using the open source software fytik [47].

The milled powders were consolidated to disc-shaped samples with 8 mm in diameter and about 1 mm in thickness by HPT. Consolidation of the powder was again performed under protective gas atmosphere for a quarter of a revolution, at an imposed pressure of 5 GPa and with a rotation speed of 1.28 rpm. The resulting disk shaped samples were then deformed by HPT for a total of 50 revolutions at room temperature, at an imposed pressure of 7.5 GPa and with a rotation speed of 1.28 rpm. The cavities of the two anvils used for deformation were sandblasted to increase friction between the sample and the anvils. To minimize the possible influence of heat generated by the high friction, the sample was cooled with compressed air during deformation. For both, powder consolidation and deformation, a hydraulic press from the company Schenk Hydraulik was used. For the parameterstudy HPT-samples with 10 revolutions, an imposed pressure of 7.5 GPa, and a rotation speed of 1.28 rpm for the composition with 10 wt.% Zn were manufactured at room temperature. After tensile testing of this samples it became apparent that 10 revolutions are not sufficient to achieve saturation of the microstructure. Thus, no further samples with 10 revolutions were produced for the other compositions.

The resulting samples were ground and polished to a thickness of around 0.5 mm. For each of the resulting discs, two tensile specimen were cut out according to the dimensions depicted in Figure 3.1(a) by a wire eroding machine. Figure 3.1(b) shows an actual sample after the tensile specimen were cut out. For each of the three compositions, as well as pure Cu, six tensile specimen were manufactured.

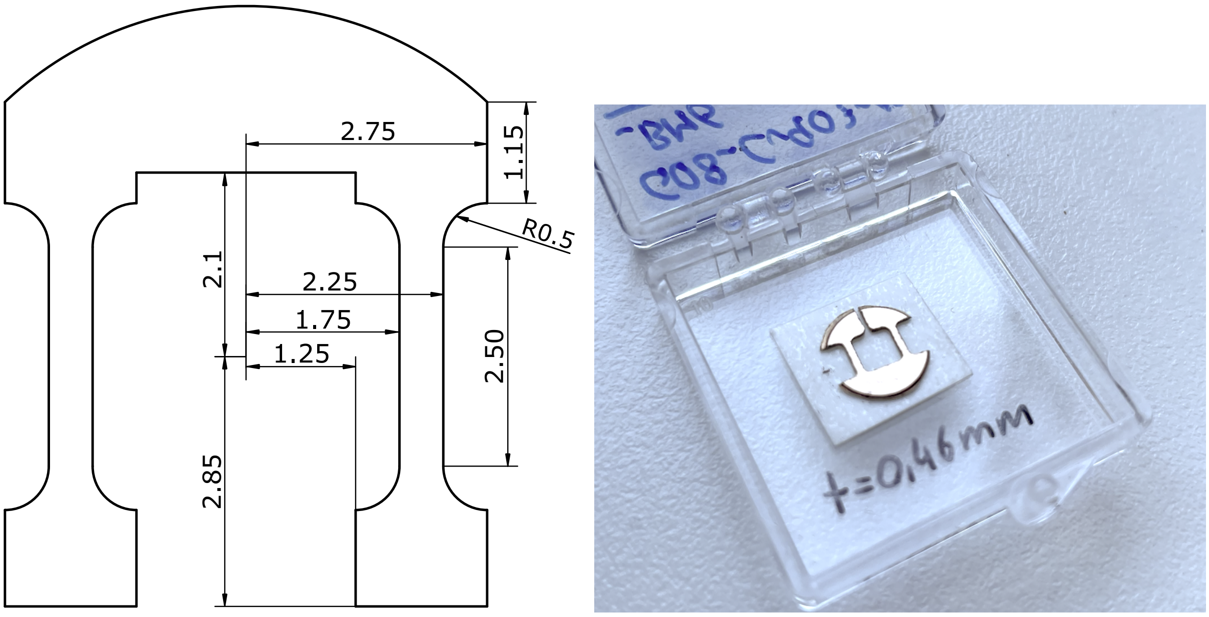

(a) (b)

Figure 3.1: Tensile specimen cut from an HPT-disk: (a) Dimensions of the tensile specimen, (b) specimen after cutting. Dimensions in (a) are given in mm.

3.2 Tensile testing

The resulting tensile specimen were tested using a Device Deformation System (DDS) and a tensile testing module from Kammrath & Weiss GmbH. Testing was performed at room temperature with a deformation speed of 2.5 µm/s and with an offset force of 5 N to stabilize the specimen before deformation. Figure 3.2 shows a tensile specimen inside the testing module right before testing. The imposed force was measured by the DDS, while the elongation of the specimen was evaluated from images that were captured during testing. Image acquisition was synchronized with the measurement of the imposed force resulting in roughly three data-pairs per second. The elongation was evaluated from the acquired images by digital image correlation (GOM correlate Pro, GOM Metrology). In the center of each end of the gauge section two points were marked using the software to track the movement throughout the images to acquire strain data for each datapoint. Calculation of the stress- and strain-values from the data, creation of the stress-strain-curves, as well as extracting of the values for yield-strength, ultimate strength, uniform elongation and total elongation from the stress strain curves were done according to the explanation in Section 2.5.

The bottom of the stress-strain curves had to be corrected due to faults by the digital image correlation caused by positioning of the samples, see Appendix A.

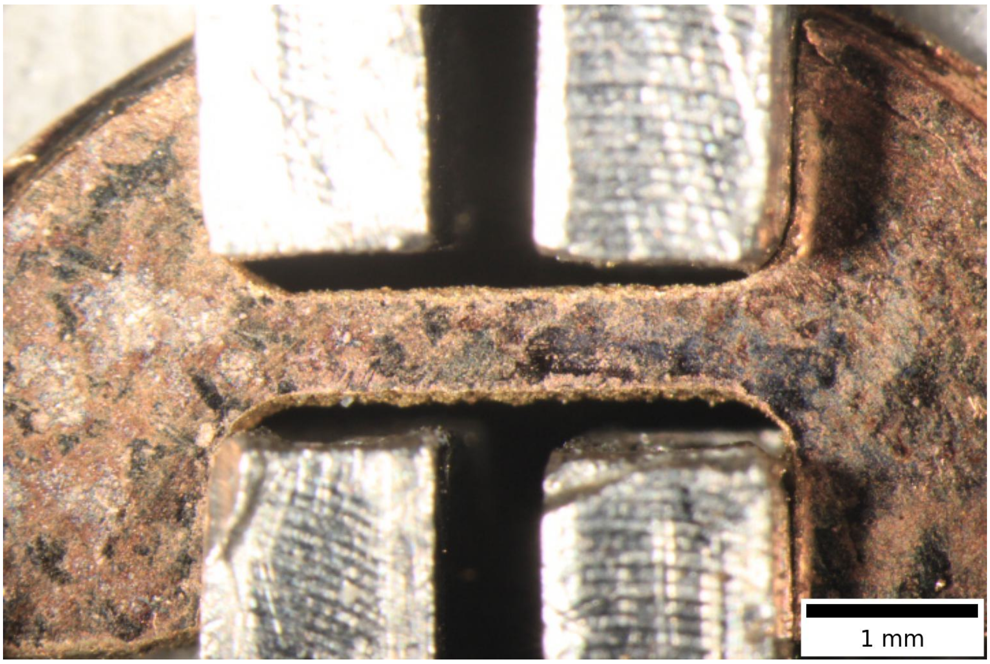

Figure 3.2: Tensile specimen inside the testing module.

Tensile samples that fractured at the head or got damaged during the fabrication process were dismissed, resulting in 4 samples for Cu100, 4 samples for Cu90Zn10, 5 samples for Cu80Zn20 and 1 sample for Cu70Zn30 that could be successfully tested.

3.3 Microstructure analysis

HPT-samples of each composition were cut in half and the microstructure was analyzed along the radius with a BSE detector situated inside a scanning electron microscope (SEM, Zeiss LEO 1525, Carl Zeiss AG). After that, the Vickers microhardness of the same HPT-samples was examined using a hardness testing device (DuraScan G5, EMCO-TEST Prüfmaschinen GmbH). Analysis of the microstructure was done to confirm the saturation of the microstructure along the radius.

TEM-samples were fabricated from the tested tensile samples at locations that correspond to the gauge section. After grinding and polishing of the respective location into a wedge shape with a tip-thickness of around 20 μm, small lamella with dimensions of 2 x 5 μm were cut out of the wedge by focused ion beam milling (SEM/FIB; Zeiss Auriga Laser platform, Carl Zeiss AG, Oberkochen, Germany). Proof of presence of deformation twins and measurement of grain size and distribution was done using a transmission electron microscope (TEM, JEOL JEM-2200FS, JEOL Ltd.). The twin density was calculated by counting the visible number of twins in the images and relate them to the average number of grains in the image, which were approximated using mean grain size and image area. Sample preparation of the TEM-samples and cutting of the lamella was done by Klemens Schmuck, and the TEM-measurements were performed by Michael Burtscher.

Chapter 4

Results and discussion

This chapter consists of two parts. The first part describes the parameterstudy to determine the optimal milling time for mechanical milling/alloying in the BM and number of revolutions during HPT deformation to ensure saturation of the microstructure for the fabricated tensile samples. The second part discusses the results obtained for the samples of different compositions by Vickers hardness measurement, tensile testing and investigation of grain size and twin density.

4.1 Part I: Parameterstudy for tensile sample fabrication

4.1.1 Ball milling

To determine the optimal milling duration for the preparation of the tensile samples, powders in the respective compositions were milled for up to 3 hours and analyzed using XRD. Results of the quantitative XRD analysis of the CuZn test powders processed by ball milling can be seen in Figure 4.1. The composition with 20 wt.% Zn is representative for the other compositions and was chosen as it best illustrates the following discussion. The reference peaks of Cu and α-CuZn are at the same 2Θ angles, hence, height changes of individual Cu or α-CuZn peaks are difficult to distinguish. The Zn peaks however, are mostly located at distinct angles. Therefore, the change in height of the Zn peaks is used as an indicator for mechanical alloying of the Cu and Zn elements.

Figure 4.2 shows a more detailed image from the diffractogramm in Figure 4.1 between the 2Θ angles of 41 and 66 degrees. It can be seen that the measured relative intensity of all the observed peaks decreases with increasing milling duration. After a total milling time of 2 hours, the peaks at $2\Theta = 42.4$, 45.6, and 64.0 degrees, which can safely be attributed to Zn, disappear. This can be explained by incorporation of the Zn in a CuZn alloy phase. Further, Figure 4.2 shows a slight peak shift to higher 2Θ angles with increasing milling time. The reason for this is believed to be the increasing compressive strain imposed on the

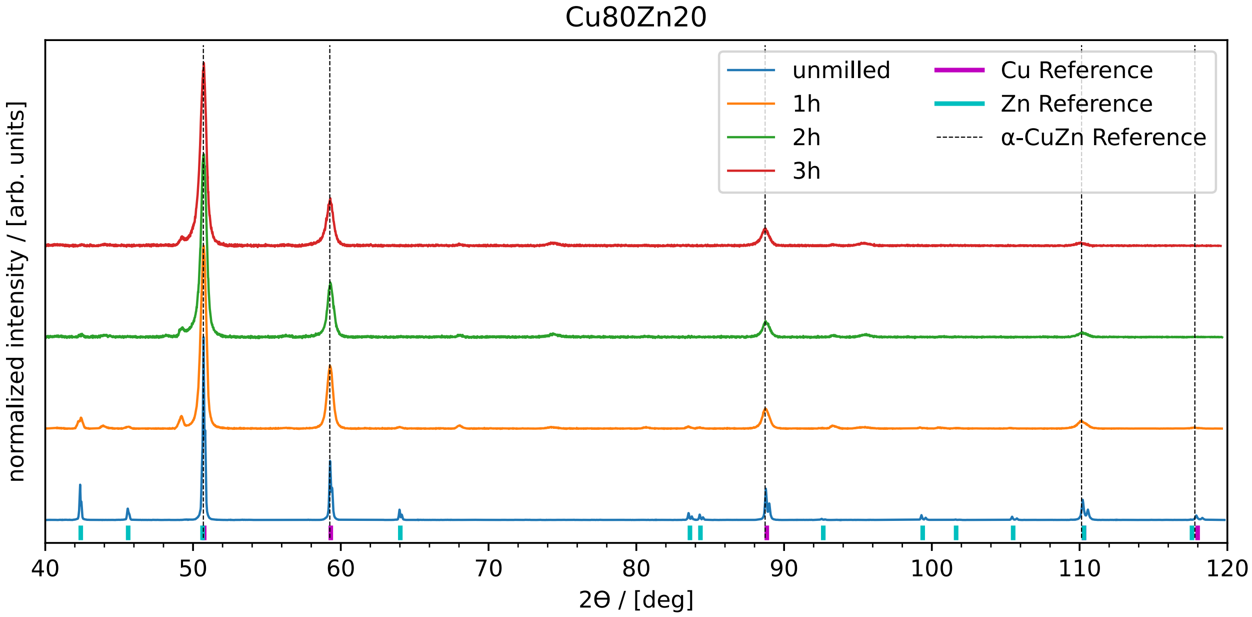

Figure 4.1: Diffractogram of a powderous sample of Cu with 20 wt.% Zn in unmilled condition, and after 1, 2, and 3 hours of ball milling.

powder particles by the ball mill. This results in a slight decrease in interplanar spacing in the crystal [43]. According to Bragg's equation, see Equation 2.13, such a decrease in lattice spacing d consequently leads to higher 2Θ angles. The fact that the unmilled powder very neatly fits the reference data backs this assumption. Another explanation is a possible difference in height of the powderous samples during XRD analysis, which can also lead to a slight offset for the 2Θ angle.

For every of the observed peaks, there is an additional smaller peak at a slightly higher angle 2Θ. These "double peaks" are assumed to be a $K_{\alpha 1}/K_{\alpha 2}$-doublet [24]. The reason for this is the presence of both, the $K_{\alpha 1}$, as well as the $K_{\alpha 2}$ wavelengths of the x-ray tube target material. Both of these wavelengths get scattered on the same lattice planes. Bragg's equation therefore mandates that the respective double peaks must be further apart with increasing angle 2Θ. This is the case, as can be seen in Figure 4.1 and Figure 4.2 by comparing peaks at different angles 2Θ, such as at 42.4 and 88.8 degrees of the unmilled powder. Another attribute of the $K_{\alpha 1}/K_{\alpha 2}$-doublet, which also applies to the observed peaks, is [24]:

$$I_{K_{\alpha 1}} : I_{K_{\alpha 2}} = 1 : 2 \tag{4.1}$$

with $I_{K_{\alpha 1}}$ and $I_{K_{\alpha 2}}$ as the exhibited intensities of the x-ray beam. As the peaks experience an intensity decrease as well as broadening with consecutive milling time, the $K_{\alpha 1}/K_{\alpha 2}$-doublets

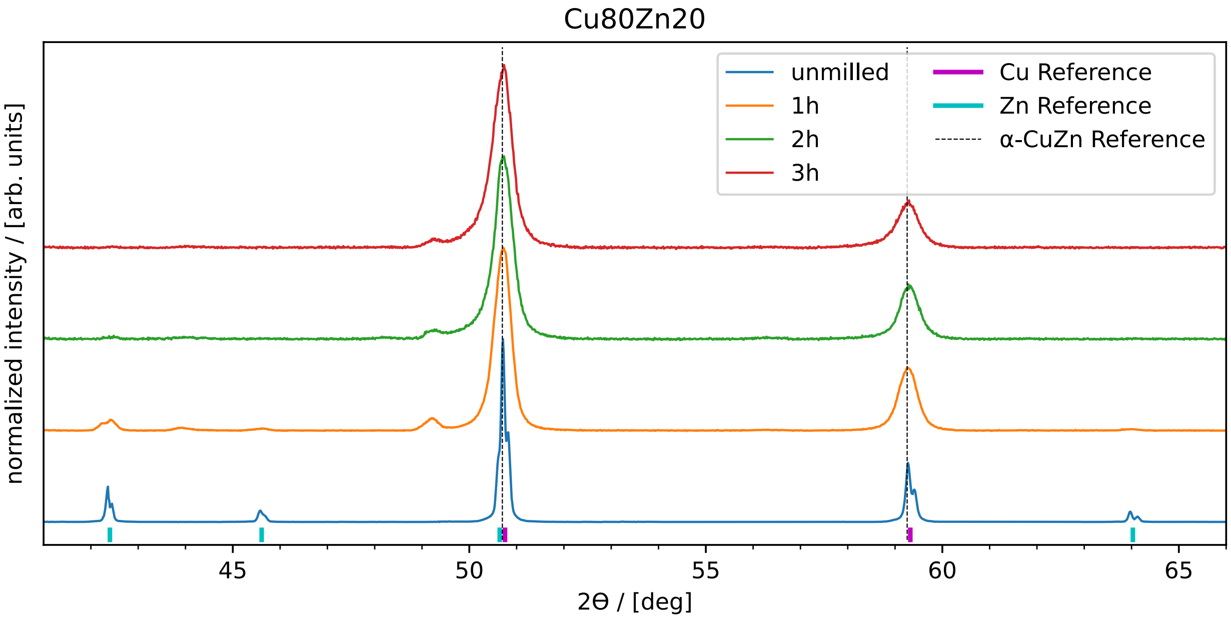

Figure 4.2: Detailed depiction of Figure 4.1.

get less distinguishable from one another. Figure 4.1 and Figure 4.2 also show peaks that are only visible for the milled powders, most notably at the angles of $2\Theta = 49.2$ and 68.1 degrees. Using the COD the peaks could be identified to be FeO and can therefore be attributed to to contamination through vial and grinding balls.

Figure 4.3 shows the FWHM analysis of the Zn peak at $2\Theta = 42.4$, 59.4, and 88.9 degrees for test powders with 10, 20, and 30 wt.% Zn over milling time. It can be seen that saturation of crystallite size occurs at roughly 30 nm after one to two hours of milling. Therefore, the milling time has been chosen to be 1.5 hours for the powders produced to fabricate the tensile samples. As mentioned in Section 2.6, it should be kept in mind that the crystallite sizes displayed in Figure 4.3 represent the lower bound of sizes present in the sample.

4.1.2 High-pressure torsion

Comparison of stress-strain curves of tensile samples made from CuZn with 10 wt.% Zn deformed by HPT for 10 and 50 revolutions are shown in Figure 4.4(b). Achieved stress and strain are both superior for the sample deformed for 50 revolutions. Figure 4.5 shows the SEM microstructure analysis of matching HPT samples at the location that corresponds to the gauge section of the tensile samples. For the sample with 10 revolutions, a certain grain elongation as well as a coarser microstructure can be observed. In addition, Figure 4.4(a) shows the measured hardness values over the radius in corresponding HPT samples with 10 wt. % Zn after 10 and 50 revolutions. It can be seen, that 10 revolutions are not sufficient to reach a state of saturation.

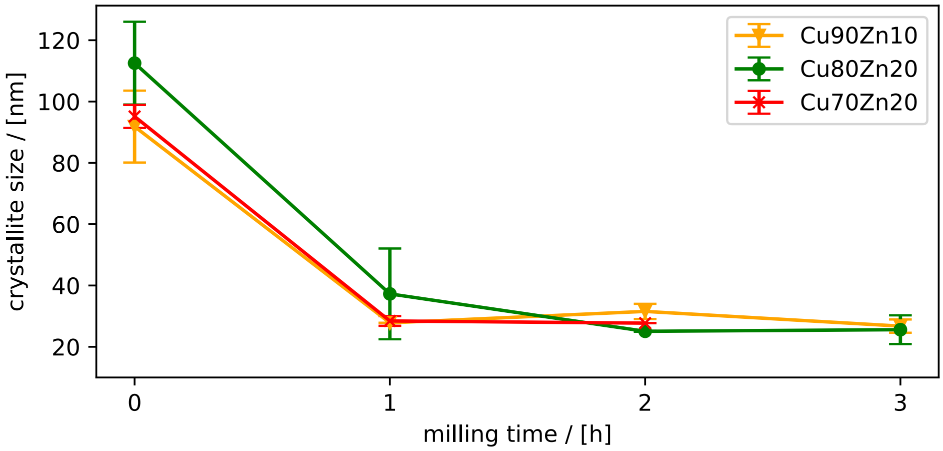

Figure 4.3: Change in crystallite size in the powderous test samples with compositions of 10, 20, and 30 wt.% Zn after consecutive milling time. Calculation was done using the FWHM from fitting of the peaks at $2\Theta = 42.4$, 59.4, and 88.9 degrees.

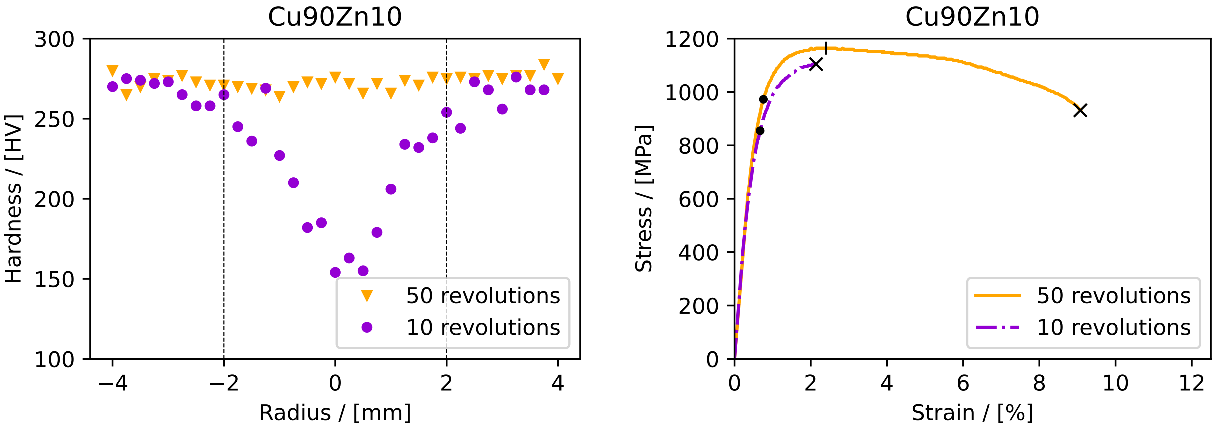

(a) (b)

Figure 4.4: Comparison of samples with 10 wt.% Zn after 10 and 50 revolutions in the HPT: (a) Measured hardness in dependence of the radius. The dashed lines represent the locations that corresponds to the gauge section of the tensile samples. (b) Representative stress-strain curves. The dots mark the yield-strength, the vertical line the uniform elongation, and the crosses the point of failure.

Because of the significantly larger total elongation exhibited by the samples with 50 revolutions compared to the ones with 10 revolutions, it can be assumed that there are additional deformation mechanisms present. Thus, it was decided to fabricate the following tensile samples with 50 revolutions in the HPT to achieve an as homogeneous as possible microstructure.

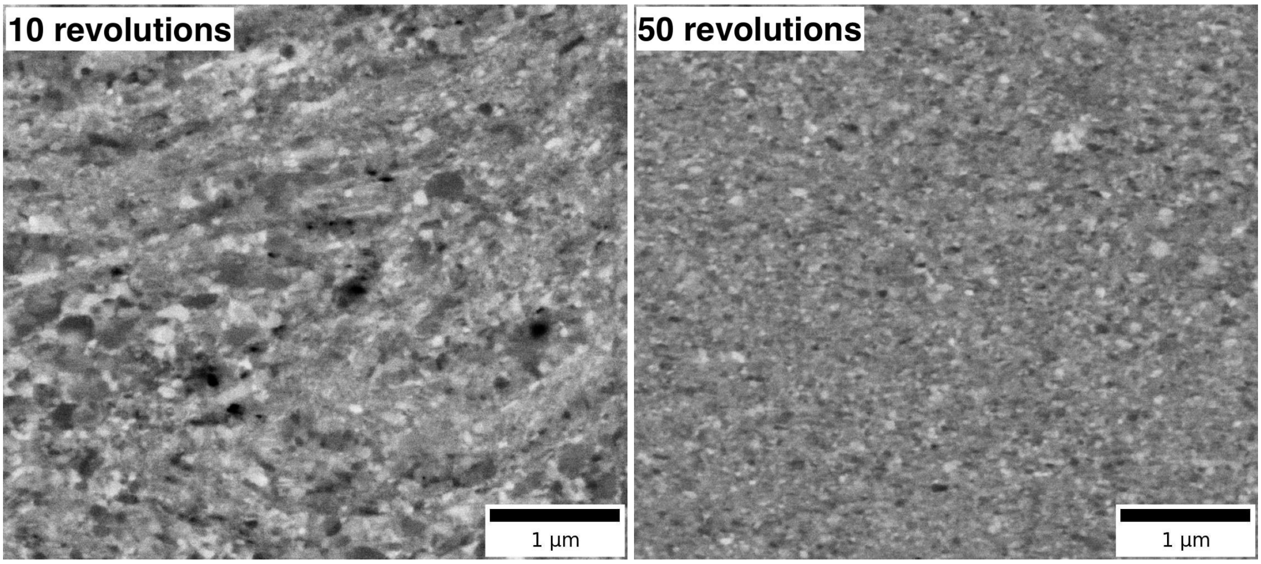

(a) (b)

Figure 4.5: SEM images of samples with 10 wt.% Zn deformed by HPT for (a) 10, and (b) 50 revolutions. The location matches the gauge section of the tensile sample, which is at a radius of 2 mm on the HPT disk.

4.2 Part II: Investigation of the different compositions

4.2.1 Microhardness testing

The measured hardness values of undeformed HPT samples for pure Cu and Cu with 10, 20, and 30 wt.% Zn are displayed in Figure 4.6. Pure Cu exhibits the lowest hardness. With increasing Zn fraction, the hardness increases as well. From the middle of the sample to a radius of 2 mm, the sample with 20 wt.% Zn shows scattering hardness values. The trend, however, is a slightly higher hardness than for bigger radii. The reason for this is assumed to be a less homogeneous microstructure at lower radii, caused by lower equivalent strain.

The 30 wt.% Zn sample behaves in a similar way, with the difference that the scattering of the hardness values spans over the whole radius. Figure 4.7 shows SEM images of the same sample at radii of 1.5, 2.0, and 2.5 mm. For all three radii, the sample displays an inhomogeneous microstructure in form of a texture. As can be seen, this seems to be independent from the radius and is therefore assumed to be the cause of the variable hardness values shown in Figure 4.6. The microstructure also differs noticeably from that of the sample with 10 wt.% Zn, which was shown in Figure 4.5(b) and exhibits much more consistent hardness values.

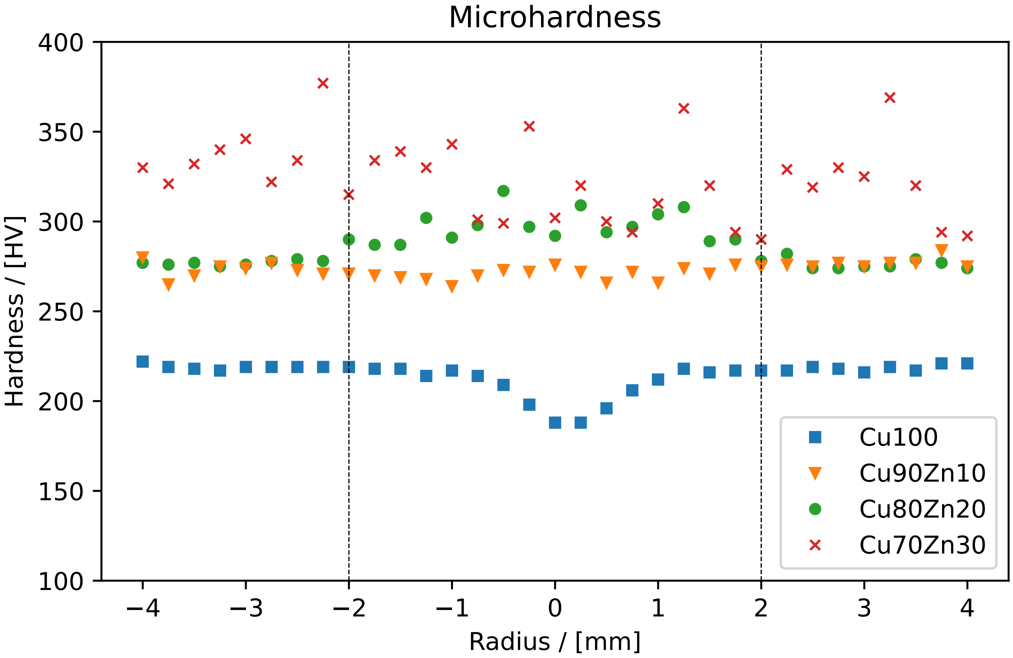

Figure 4.6: Measured Hardness values for undeformed HPT samples of pure Cu an 10, 20, and 30 wt.% Zn after 50 revolutions by HPT along the radius. The dashed line at radii of 2 and -2 mm represent the location that corresponds to the gauge section of the tensile samples.

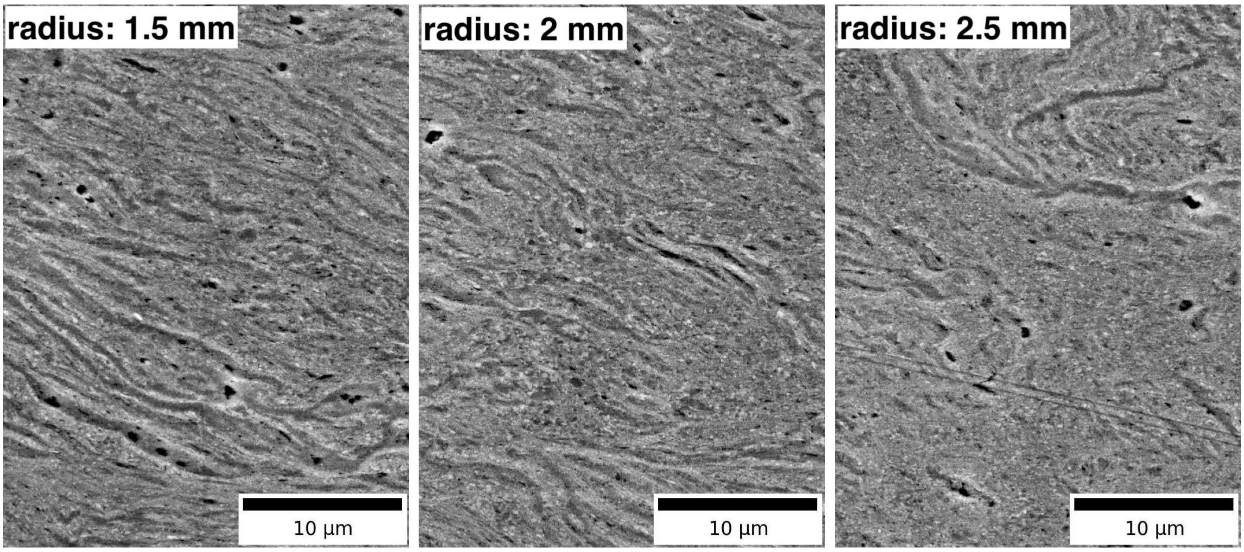

(a) (b) (c)

Figure 4.7: SEM images of samples with 30 wt.% Zn deformed for 50 revolutions by HPT at a radius of (a) 1.5 mm, (b) 2.0 mm, and (c) 2.5 mm. Regardless of radius, this composition shows an inhomogeneous microstructure.

4.2.2 Tensile testing

Stress-strain curves from representative tensile testing experiments of pure Cu and CuZn samples with 10, 20, and 30 wt.% Zn can be seen in Figure 4.8(a). Curves of all successful tested samples for the respective compositions are depicted in Figure 4.8(b) , 4.8(c), and 4.8(d). From the manufactured samples with 30 wt.% Zn, only one could be tested successfully, as the majority of samples with this composition failed brittle near the heads before a meaningful part of the curve could be measured; its curve can be seen in Figure 4.8(a). The highest elongation to failure is exhibited by pure Cu samples followed by the CuZn samples with 10 wt.% Zn. The ultimate strength is highest in the samples with 10 wt.% Zn. According to literature, the stacking fault energy γ_{SF} in CuZn alloys decreases with increasing Zn content (45 mJ/m^2 in pure Cu to 14 mJ/m^2 in CuZn with 30 wt.% Zn [19, 28]), which promotes mechanical twinning [8, 48, 49]. Figure 4.8(a) shows that yield-strength and ultimate strength increase until a Zn content of 10 wt.% before starting to decrease again, with the 20, and 30 wt.% Zn samples being significantly more brittle than the other two. The CuZn samples with 30 wt.% Zn started to break shortly after starting the tensile testing, thus, it was not possible to obtain usable mechanical properties for these samples. Table 4.1 shows the obtained values for yield-strength $\sigma_{0.2}$, uniform elongation ϵ_u, total elongation ϵ_t, and mean grain size d_{mean} including standard deviation, as well as Vickers hardness H.

Table 4.1: Mean measured values including standard deviation of yield-strength $\sigma_{0.2}$, uniform elongation ϵ_u, total elongation ϵ_t, and mean grain size d_{mean} as well as Vickers hardness H that corresponds to the gauge section of the tensile samples for pure Cu and CuZn samples with 10, 20, and 30 wt.% Zn.

Samples	**Cu100**	**Cu90Zn10**	**Cu80Zn20**	**Cu70Zn30**
$\sigma_{0.2}$ / [MPa]	590 ± 20	960 ± 30	870 ± 50	-
ϵ_u / [%]	3.2 ± 0.1	1.9 ± 0.2	-	-
ϵ_t / [%]	11.3 ± 0.4	8.9 ± 0.7	0.9 ± 0.5	0.2
H / [HV]	220	270	280	320
d_{mean} / [nm]	69 ± 33	53 ± 23	37 ± 20	-

Several differences can be observed compared to the results from Zhao *et al.* [8] shown in literature. The measured uniform elongation ϵ_u of the 10 wt.% Zn sample in this work with 1.9 ± 0.2% is lower as the representative reference sample from Zhao *et al.* with 2.5%. In contrast to this, all other measured mechanical properties in this work are higher for the samples with a composition of up to 10 wt.% Zn than that of Zhao *et al.*. The exhibited total elongation ϵ_t from the pure Cu samples, for example, is 11.3 ± 0.4% (this work) compared to 4.9% (Zhao *et al.*). This also applies to the measured yield-strength $\sigma_{0.2}$, with measured values of 590 ± 20 and 960 ± 30 MPa compared to the literature values of 420 and 580 MPa for pure Cu and the composition with 10 wt.% Zn. The sample with 30 wt.% Zn, however,

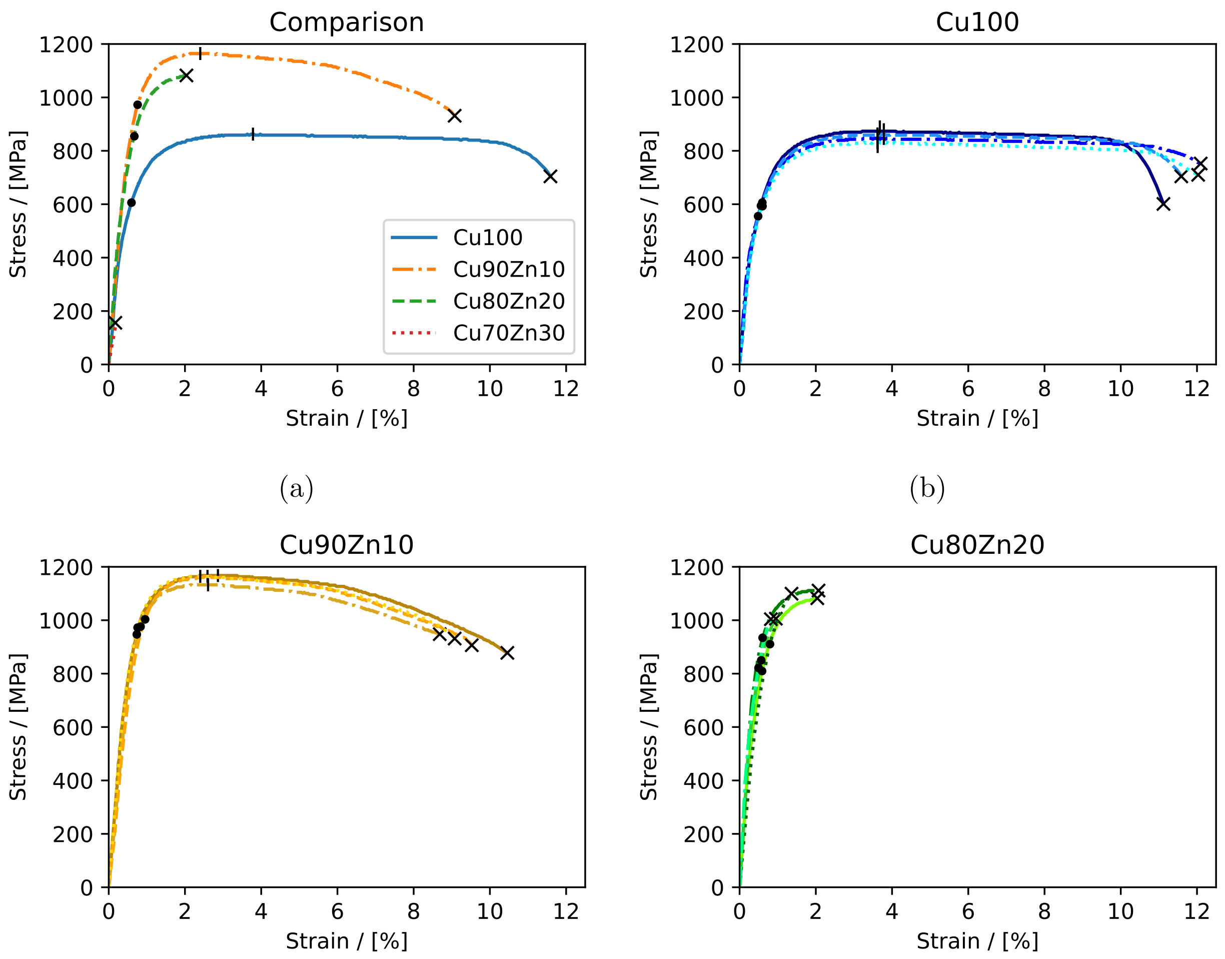

(a)

(b)

(c)

(d)

Figure 4.8: Comparison of stress-strain curves from of the tensile samples fabricated by HPT discs deformed for 50 revolutions: (a) representative curves for tensile samples of pure Cu and CuZn with 10, 20, and 30 wt.% Zn, and stress-strain curves from (b) pure Cu samples, (c) samples with 10 wt.% Zn, and (d) samples with 20 wt.% Zn. The dots mark the yield-strength, the vertical lines the uniform elongation, and the crosses the point of failure.

is the one which exhibits the lowest ultimate strength σ_u, and is to brittle for proper tensile testing with this experimental setup.

4.2.3 Grain size and twin density measurements

The samples from this work in general exhibit higher tensile strengths, with the 20 and 30 wt.% Zn samples being more brittle than the ones from Zhao *et al.* [8]. This hints at increased hardening during the fabrication process, which seems plausible considering the higher number of 50 revolutions during HPT deformation, and should therefore be observable in smaller grain sizes in the sample. Figure 4.9 shows grain size distributions and average grain size, as well as cumulative grain sizes for the tested tensile samples done by TEM. The measured values again deviate significantly from the results from Zhao *et al.*, with an average grain sizes as low as 69 ± 33 nm compared to 180 nm for the pure Cu samples, and 53 ± 23 nm compared to 110 nm for the samples with 10 wt.% Zn. This result fits the higher observed total elongations for the pure Cu sample and the sample with 10 wt.% Zn, as a smaller grain size promotes deformation by twinning. At the same time, the majority of the grains are still bigger than the critical value of 10 to 20 nm, consequently not triggering the reverse Hall-Petch behavior.

The only sample that shows a meaningful percentage of grains smaller than the reported threshold for the reverse Hall-Petch behavior is the one with 20 wt.% Zn. This poses a possible explanation for the higher exhibited hardness values for lower radii by this sample, which is displayed in Figure 4.6. With higher shear strain at higher radii leading to smaller grains and thus to lower hardness and strength values.

Samples with smaller mean grain size exhibited smaller uniform and total elongations during tensile testing, see Figure 4.8. This observation is consistent with the literature, as smaller grains can contain increasingly less dislocations.

Similar to Zhao *et al.* [8], the average grain size, as well as the width of the grain size distribution decreases with increasing fraction of Zn, and therefor with decreasing stacking fault energy γ_{SF}. Comparison between the grain sizes distribution and the FWHM calculation in Section 4.1.1 indicates that the saturation of the grain size after HPT can not be reached with ball milling alone. The lower bound crystallite size determined after ball milling, see Section 4.1.1, saturates at around 30 nm. Figure 4.9(d) shows that, with increasing Zn content, there is a meaningful amount of grains smaller than 30 nm. In case of the composition with 20 wt.% Zn, even almost half of the grains. This observation is consistent with the microhardness measurement seen in Figure 4.4(a), which indicates that HPT deformation is necessary to achieve small grain size a saturated microstructure in the samples.

Figure 4.10 shows TEM images of deformed tensile samples of pure Cu, and CuZn with 10 and 20 wt.% Zn. In contrast to Zhao *et al.* [8], deformation twins are present in the pure Cu sample as well. This is consistent with the more than doubled total elongation exhibited by the pure Cu samples in this work. The main reason for this is believed to be the significantly

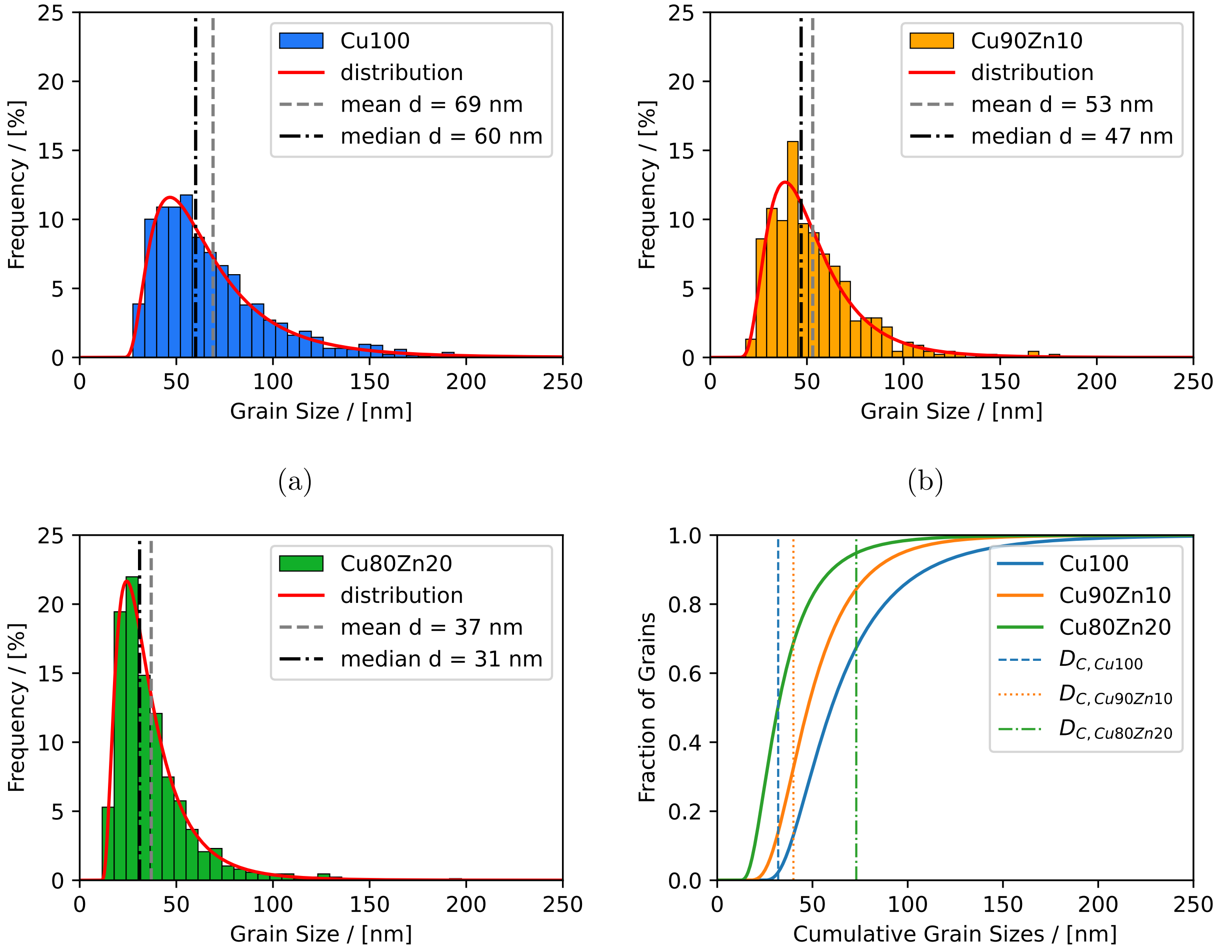

(a) (b)

(c) (d)

Figure 4.9: Grain size distributions and mean grain sizes of (a) pure Cu, samples with (b) 10, and (c) 20 wt.% Zn, and (d) cumulative grain size distribution with critical grain sizes D_C.

lower mean grain size of 69 ± 33 nm compared to Zhao *et al.* (180 nm), which promotes deformation by twinning.

The measured twin densities β and mean grain sizes d_{mean} of the tested tensile samples of pure Cu, and samples with 10, and 20 wt.% Zn after tensile testing compared to the respective measurements of Zhao *et al.* [8] are listed in Table 4.2, and generally fit the results from the tensile experiments. Pure Cu, which showed the highest uniform elongation ϵ_u, also exhibits the highest twin density of 7.1 ± 1.9%. This result stands in contrast to the work of Zhao *et al.*, where with 0.1%, the pure Cu sample exhibits almost no twin density at all. The main cause of this contradiction is believed to be caused by the huge difference in grain size from the two samples. With a mean grain size of 69 ± 33 nm in contrast to 180 nm from Zhao *et al.*, the pure Cu sample from this work is much closer to the as ideal reported grain size of 46 nm. The distribution in Figure 4.9(a) shows that almost 20% of grains are close to the desired size, which therefore greatly benefits deformation by twinning.

Figure 4.10(d) shows a TEM image of the microstructure from a CuZn sample with 10 wt.% Zn. The green lines in the images represent the observed twins in the sample and were drawn for better visualization. A majority of the observed twins lie in smaller grains with sizes of approximately 40 to 60 nm, which fits the trend of the grain size effect for twinning discussed in Section 2.2.3.

Table 4.2: Measured mean grain sizes d_{mean} and twin densities including standard deviation of pure Cu and CuZn samples with 10 and 20 wt.% Zn after tensile testing with the respective results from Zhao *et al.*.

samples	**Cu100**	**Cu90Zn10**	**Cu80Zn20**
d_{mean} / [nm]	69 ± 33	53 ± 23	37 ± 20
$d_{mean\,Zhao\,et\,al.}$ / [nm]	180	110	-
β / [%]	7.1 ± 1.9	6.5 ± 1.7	4.6 ± 0.9
$\beta_{Zhao\,et\,al.}$ / [%]	0.1	5.5	-

The sample with 10 wt.% Zn exhibits a twin density of 6.5 ± 1.7%, a slightly higher mean value than the 5.5% from the respective sample from Zhao *et al.* [8]. This again fits the results from the tensile experiments, which indicates that the high measured elongations are indeed enabled by twinning. As with the pure Cu sample, the mean grain size also lies in the desired size range. The sample with 20 wt.% Zn exhibits a twin density of 4.6 ± 0.9%. Since there is no equivalent sample from Zhao *et al.*, it can not be directly compared. It is apparent that, although the sample exhibits a meaningful twin density of 4.6 ± 0.9%, it is rather brittle and does not show significant plastic elongation in the tensile experiments. A possible explanation for this would be the very small mean grain size of only 37 ± 20 nm, which is not only possibly past its reported ideal grain size for twinning (between 35 and 45 nm), but also causes significant hardening according to the Hall-Petch relationship.

Unfortunately, the measured twin densities do not correlate with the critical grain sizes calculated in subsection 2.2.3, as the results would predict the highest twin density for the samples with 30 wt.% Zn and the lowest for pure Cu.

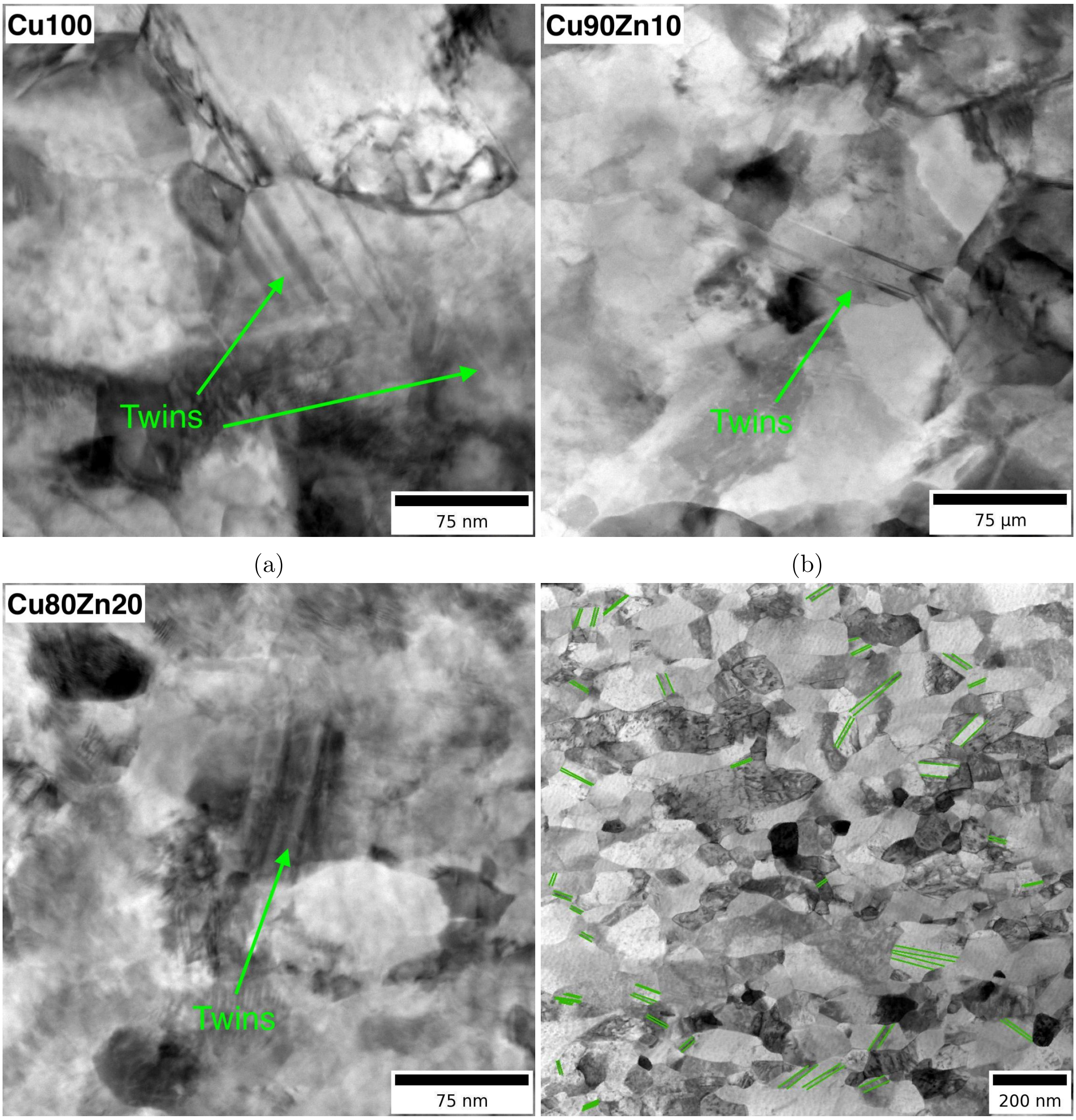
Cu100
Twins
75 nm
Cu90Zn10
Twins
75 µm
Cu80Zn20
Twins
75 nm
200 nm

(a) (b)

(c) (d)

Figure 4.10: TEM images of twins in the deformed tensile samples of (a) pure Cu, and samples with (b) 10, (c) 20 wt.% Zn and (d) overview of several twinned grains in the sample with 10 wt.% Zn. The green lines in (d) mark the recognized twin boundaries used for calculation of the twin densities.

Chapter 5

Conclusions

A powder based route consisting of processing by ball milling and subsequent HPT deformation was used to manufacture tensile samples from pure Cu and CuZn alloys with 10, 20, and 30 wt.% Zn. XRD analysis was done to determine the optimal milling duration for the ball mill to ensure an as small as possible crystallite size of the milled powder, and was concluded to be 1.5 h for saturation.

A number of 50 revolutions during manufacturing by HPT leads to grain sizes within the nanocrystalline regime in all compositions. TEM investigations were used to measure the mean grain size, which was determined to be 69 nm, 53 nm, and 37 nm for the sample compositions of pure Cu, and 10 and 20 wt.% Zn, respectively. The grain sizes are close to the reported ideal grain size for deformation twinning in Cu and the respective CuZn alloys. The twin density was determined from the TEM investigations in the deformed state after tensile testing resulting into densities of 7.1% for pure Cu, 6.5% for 10 wt.% Zn, and 4.6% for the 20 wt.% compositions, respectively. The measured twin densities for the tested samples fit their respective exhibited elongations, which is seen as strong indication for deformation twinning actually being the dominating deformation mechanism. They do not however match the calculated critical grain sizes. This may be due to inconsistent reported values for the stacking fault energy and/or simplifications of the model. Comparing the tensile testing results with literature values obtained by Zhao *et al.* [8], shows an up to 30% increase in strength, and, except for pure Cu, a reduced uniform elongation. The increased strength might stem from the smaller grain sizes compared to the values given by Zhao *et al.*. From the comparison it became apparent that even for the same composition, and therefore the same stacking fault energy, the grain size seems to be the critical component that must be mastered to achieve NC materials with the desired combination of high strength and high ductility.

Chapter 6

Outlook

A key advantage of a powder based manufacturing route lies in easier customization of the material composition. Alloys manufactured this way can therefore much easier be used in composite materials. The combination of an alloy as shown in this work with a high strength component can therefore lead to composites with decent ductility without sacrificing too much of its strength. Further investigation should be conducted on the optimal and critical grain size for the respective compositions, as calculations and experimental observations seem to deviate, especially for higher fractions of Zn content. Reliable values for stacking fault energy will be needed to accurately predict these grain sizes. High temperatures during HPT deformation can also be used to further fine tune the grain size, as the ideal grain sizes are reported to be higher for the compositions with increased Zn fraction. As proposed by Zhu *et al.* [4], controlled annealing could also be used after HPT deformation to reduce the defect density and recover some of the work hardening.

Another step will be the combination of the CuZn alloy with 10 wt.% Zn with W to achieve even higher mechanical properties, and to increase the fracture tolerance of W in a nanocomposite. A powder based manufacturing route not only enables much easier production of samples, but also easier tailoring of an eventually produced final product.

References

[1] C. Suryanarayana, Bulletin of Materials Science **17**, 307 (1994).

[2] Y. Wang, M. Chen, F. Zhou, and E. Ma, Nature **419**, 912 (2002).

[3] Y. T. Zhu and X. Liao, Nature Materials **3**, 351 (2004).

[4] Y. Zhu, X. Liao, and X. Wu, Progress in Materials Science **57**, 1 (2012).

[5] C. C. Koch, Journal of Materials Science **42**, 1403 (2007).

[6] F. A. Mohamed and H. Yang, Metallurgical and Materials Transactions A **41**, 823 (2010).

[7] M. A. Meyers, A. Mishra, and D. J. Benson, Progress in Materials Mcience **51**, 427 (2006).

[8] Y. Zhao, X. Liao, Z. Horita, T. Langdon, and Y. Zhu, Materials Science and Engineering: A **493**, 123 (2008).

[9] K. Youssef, M. Sakaliyska, H. Bahmanpour, R. Scattergood, and C. Koch, Acta Materialia **59**, 5758 (2011).

[10] D. Jia, Y. Wang, K. Ramesh, E. Ma, Y. Zhu, and R. Valiev, Applied Physics Letters **79**, 611 (2001).

[11] D. Hull and D. J. Bacon, *Introduction to dislocations* (Butterworth-Heinemann, 2011).

[12] G. Gottstein, *Physical foundations of materials science* (Springer Science & Business Media, 2013).

[13] P. M. Anderson, J. P. Hirth, and J. Lothe, *Theory of dislocations* (Cambridge University Press, 2017).

[14] Y. T. Zhu and T. G. Langdon, Materials Science and Engineering: A **409**, 234 (2005).

[15] M. Y. Gutkin, I. Ovid'Ko, and N. Skiba, Acta Materialia **51**, 4059 (2003).

[16] A. H. Chokshi, Scripta Materialia **34**, 1905 (1996).

[17] J. Weertman, D. Farkas, K. Hemker, H. Kung, M. Mayo, R. Mitra, and H. Van Swygenhoven, Mrs Bulletin **24**, 44 (1999).

[18] M. Zhao and Q. Jiang, in *2006 IEEE Conference on Emerging Technologies-Nanoelectronics* (IEEE, 2006) pp. 472–474.

[19] X. An, S. Wu, Z. Wang, and Z. Zhang, Progress in Materials Science **101**, 1 (2019).

[20] J. Schiøtz, F. D. Di Tolla, and K. W. Jacobsen, Nature **391**, 561 (1998).

[21] H. Van Swygenhoven and J. R. Weertman, Materials today **9**, 24 (2006).

[22] E. El-Danaf, S. R. Kalidindi, and R. D. Doherty, Metallurgical and Materials Transactions A **30**, 1223 (1999).

[23] Y. Zhu, X. Liao, X. Wu, and J. Narayan, Journal of Materials Science **48**, 4467 (2013).

[24] V. Pecharsky and P. Zavalij, *Fundamentals of Powder Diffraction and Structural Characterization of Materials (2nd Version)* (Springer Science & Business Media, 2009).

[25] M. Chen, E. Ma, K. J. Hemker, H. Sheng, Y. Wang, and X. Cheng, Science **300**, 1275 (2003).

[26] J. Hua and A. Hartmaier, in *Journal of Physics: Conference Series*, Vol. 240 (IOP Publishing, 2010) p. 012010.

[27] N. Nunomura, Information Technology Center, University of Toyama **9**, 35 (2012).

[28] X. Ma, W. Xu, H. Zhou, J. Moering, J. Narayan, and Y. Zhu, Philosophical Magazine **95**, 301 (2015).

[29] E. A. El-Danaf, A. Al-Mutlaq, and M. S. Soliman, Materials Science and Engineering: A **528**, 7579 (2011).

[30] Y. Zhu, X. Liao, S. Srinivasan, and E. Lavernia, Journal of Applied Physics **98**, 034319 (2005).

[31] X. Liao, Y. Zhao, S. Srinivasan, Y. Zhu, R. Valiev, and D. Gunderov, Applied physics letters **84**, 592 (2004).

[32] Y. Cao, Y. Wang, Z. Chen, X. Liao, M. Kawasaki, S. Ringer, T. Langdon, and Y. Zhu, Materials Science and Engineering: A **578**, 110 (2013).

[33] A. Rohatgi, K. S. Vecchio, and G. T. Gray, Metallurgical and Materials Transactions A **32**, 135 (2001).

[34] M. Abdellaoui and E. Gaffet, Acta Metallurgica et Materialia **43**, 1087 (1995).

[35] C. Suryanarayana, Progress in Materials Science **46**, 1 (2001).

[36] C. Suryanarayana, E. Ivanov, and V. Boldyrev, Materials Science and Engineering: A **304**, 151 (2001).

[37] A. Hohenwarter, A. Bachmaier, B. Gludovatz, S. Scheriau, and R. Pippan, International Journal of Materials Research **100**, 1653 (2009).

[38] K. S. Kormout, R. Pippan, and A. Bachmaier, Advanced Engineering Materials **19**, 1600675 (2017).

[39] R. Pippan, S. Scheriau, A. Taylor, M. Hafok, A. Hohenwarter, and A. Bachmaier, Annual Review of Materials Research **40**, 319 (2010).

[40] R. Pippan, A. Hohenwarter, S. Scheriau, and A. Bachmaier, Physik in unserer Zeit **41**, 23 (2010).

[41] M. Wurmshuber, S. Doppermann, S. Wurster, and D. Kiener, in *IOP Conference Series: Materials Science and Engineering*, Vol. 580 (IOP Publishing, 2019) p. 012051.

[42] J. R. Davis, *Tensile testing* (ASM international, 2004).

[43] M. Lee, *X-Ray diffraction for materials research: from fundamentals to applications* (CRC Press, 2017).

[44] E. Zolotoyabko, *Basic concepts of X-ray diffraction* (John Wiley & Sons, 2014).

[45] B. J. Inkson, in *Materials characterization using nondestructive evaluation (NDE) methods* (Elsevier, 2016) pp. 17–43.

[46] A. Vaitkus, A. Merkys, and S. Gražulis, Journal of applied crystallography **54**, 661 (2021).

[47] M. Wojdyr, Journal of Applied Crystallography **43**, 1126 (2010).

[48] C. Carter and I. Ray, Philosophical Magazine **35**, 189 (1977).

[49] L. Balogh, T. Ungár, Y. Zhao, Y. Zhu, Z. Horita, C. Xu, and T. G. Langdon, Acta Materialia **56**, 809 (2008).

Appendix

A Extrapolation of Stress-Strain Curves

Elongations evaluated from digital image correlation showed negative values at the beginning of the curve. This is believed to be caused by deviations from the ideal symmetric dimensions of the tensile samples. As mentioned in Section 3.2, the tensile samples wer stabilized before deformation with an offset force of 5 N. As the sample is exposed to further tensile stress, it seems that it starts to further align towards a perfectly horizontal orientation, suggesting that this was not the case prior to testing. Causing a slight shift due to not perfectly symmetric shoulders of the sample, this motion of the is then recognized in the evaluation as a negative elongation, thus requiring some corrections to the measured curve.

It was therefore decided to correct the faulty section of the elastic part of the curve by linear extrapolation to get a more accurate stress-strain-curve. The decision for the linear extrapolation is based on two assumptions:

1. A negative elongation is not possible in tensile testing, and
2. Hook's law dictates that the stress σ is proportional to the strain ϵ in the elastic part of the stress-strain curve [12].

Every curve was first cropped by the faulty part, then linear extrapolated and moved to the origin of the plot. Depending on the curve, between 20 and 100 data points were used for extrapolation. Figure A.1 shows an example of a measured and a corrected curve.

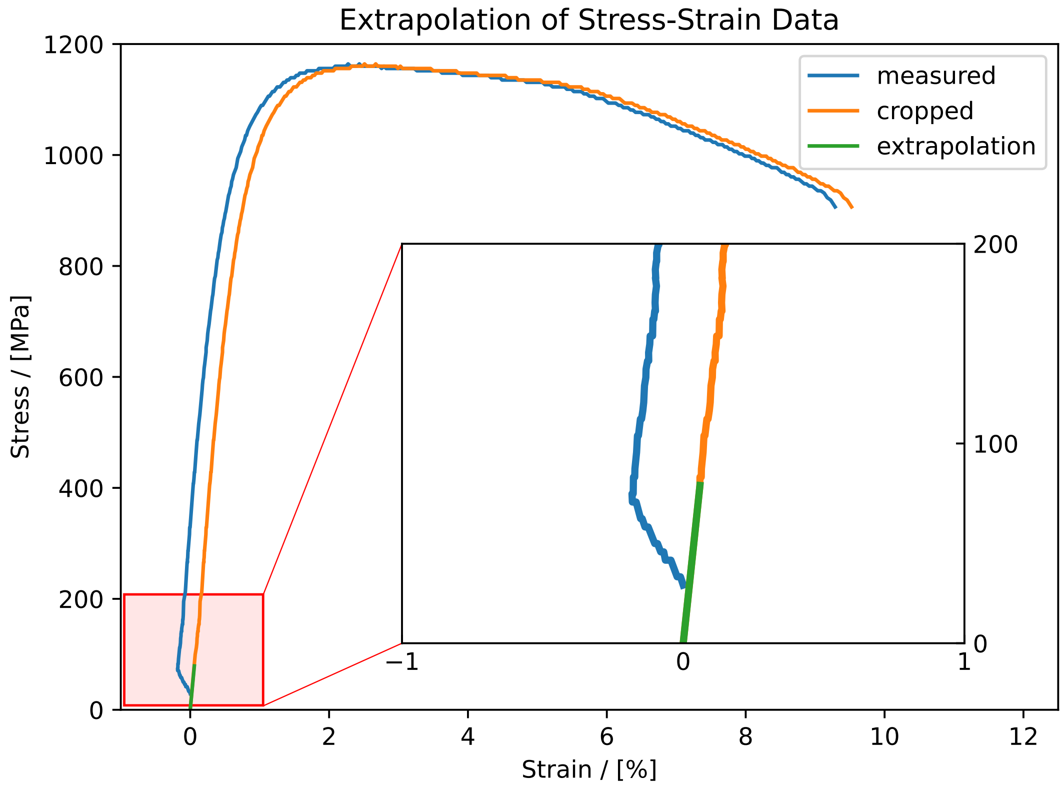

Figure A.1: Depiction of an example of the difference between measured and corrected curve. The blue line represents the as measured curve, the orange line the cropped curve, and the green line the linear extrapolation for the cropped part.